Mature diffuse tectonic block boundary revealed by the 2020 southwestern Puerto Rico seismic sequence

U.S. ten Brink[1*], L. Vanacore[2], E.J. Fielding[3], J.D. Chaytor[1], A.M. López-Venegas[2], W. Baldwin[1], D. Foster[1], B.D. Andrews[1]

1 – U.S. Geological Survey, Woods Hole Science Center, Woods Hole, MA

2 – Dept. of Geology, U. of Puerto Rico, Mayaguez, PR

3 – Jet Propulsion Laboratory, California Institute of Technology, Pasadena, CA

* Corresponding author: Uri ten Brink utenbrink@usgs.gov

Revised October 12, 2021

Key points

-Seismic activity did not follow main shock-aftershock sequence and likely ruptured multiple faults in southwest Puerto Rico

-Geologic indicators suggest long-term diffuse deformation due perhaps to heterogenous arc composition

-This zone may be the southernmost domain of a diffuse deformation boundary between Hispaniola and Puerto Rico

Abstract

Distributed faulting typically tends to coalesce into one or a few faults with repeated deformation. The 2020 seismic sequence in southwestern Puerto Rico (SWPR) was characterized however by rupture of several short intersecting strike-slip and normal faults. The deformation does not appear to have coalesced despite several lines of geological and morphological evidence suggesting repeated deformation since post early Pliocene (~>3 Ma). The progression of clustered medium-sized (≥Mw4.5) earthquakes, modeling shoreline subsidence from InSAR, and sub-seafloor mapping by high-resolution seismic reflection profiles, suggest that the earthquake swarm was distributed across several fault planes beneath the insular shelf and upper slope in the vicinity of Guayanilla submarine canyon. The deformation may represent the southernmost part of a diffuse boundary, the Western Puerto Rico Deformation Boundary, which accommodates differential movement between the Puerto Rico and Hispaniola arc blocks. This differential movement is possibly driven by the differential seismic coupling along the Puerto Rico – Hispaniola subduction zone. We propose that the compositional heterogeneity across the island arc retards the process of focusing the deformation into a single fault. Given the evidence presented here, we should not expect a single large event in this area but similar diffuse sequences in the future.

1. Introduction

The 2019-2020 seismic swarm in southwestern Puerto Rico (SWPR) (Fig. 1) consisted of +13,000 earthquakes (M≥2.5) with 43 earthquakes with Mw ≥ 4.5 since its start on December 28, 2019. The largest of these events, an Mw6.4 on January 7, 2020 was located offshore and had a mixed normal and strike-slip motion (*Liu et al.*, 2020, ANSS-ComCat). The earthquake sequence and in particular the Mw6.4 earthquake caused extensive damage in coastal towns (*Morales-Velez et al.*, 2020; *Miranda et al.*, 2020; *Von Hillebrandt et al.*, 2020), co-seismic subsidence around Guayanilla Bay (*Allstadt et al.*, 2020; *Fielding et al.*, 2020; *Pérez-Valentín et al.,* 2021), liquefaction, ground failures, and the collapse of an iconic coastal rock bridge (*López-Venegas et al.*, 2020a, 2020b, *Allstad et al.*, 2020; *Pérez-Valentín et al.,* 2021). The prolonged seismic activity had thus created anxiety among the island's population. The activity was centered around a defunct oil refinery and strategic facilities for the island, such as a liquid natural gas terminal, and an electric power station.

This seismic activity as expressed in the earthquakes' b-value is not a typical foreshock, main shock, and aftershock sequence (*Dascher-Cousieau et al.*, 2020). Based on the time series of the b-values, Dascher-Cousieau et al. (2020) interpreted this earthquake activity to indicate that the observed seismic activity to date is part of a foreshock sequence with a larger main shock yet to come. An alternative view which we discuss here is that the seismic activity represents the rupture of many faults, that are part of a diffuse block boundary within the Greater Antilles island arc. A similar diffuse block boundary and associated sequences of seismic activity had been suggested for the 70-100-km-wide Central Costa Rica Deformed Belt across the Costa Rica volcanic arc, which separates the middle America subduction zone from the Panama Block (*Marshall et al.*, 2000).

We address the following questions: 1. Can we identify the faults responsible for the 2019-2020 seismic sequence?.2 Is the activity organized in a predictable way? 3. Is it a recurring activity? 4. What framework tectonics generated this activity?

Most of the activity during this sequence occurred offshore. Mapping faults relied on several lines of evidence: (a) Mapping faults in the shallow sub-seafloor by marine high-resolution seismic reflection survey and evaluating seafloor geomorphology; (b) Matching vertical and horizontal displacement models to observed InSAR coastal deformation around the January 7, 2020 Mw6.4 earthquake and the July 3, 2020 Mw5.3 earthquake; (c) Identifying clusters of medium earthquakes and drawing possible faults based on their focal mechanisms.

2. Background

Bedrock in Puerto Rico and Hispaniola formed as part of the inactive Mesozoic and early Cenozoic Greater Antilles island arc that accommodated southwestward subduction of the North American plate under the Caribbean plate. Subduction direction changed to WSW starting ~40 Myr ago (*Pindell and Kennan*, 2009) resulting in a very oblique convergence along the trench north of Puerto Rico (Fig. 1; *DeMets et al.*, 2000). Muertos Trough, a wedge of deformed sediment south of the island accommodates thrusting of the arc over the interior Caribbean plate, likely in a sub-perpendicular orientation to the trough (*ten Brink et al.*, 2009).

The 2020 seismic sequence occurred mostly within the insular shelf and slope south of Puerto Rico (Fig. 1). The slope there is dissected by the tributaries of Guayanilla Canyon, which cuts down through unconsolidated Quaternary deposits, the middle Miocene to Early Pliocene shelf carbonates of the Ponce Formation, and the deeper Juan Diaz Formation chalks (*Trumbull and Garrison*, 1973). The Guayanilla canyon system is the only significant submarine drainage along the south coast of Puerto Rico. The canyon system has eroded into the insular shelf, forming an asymmetric amphitheater (Fig. 1 and 2). West and east of this canyon system, the shelf edge is oriented roughly W-E and canyon systems are largely absent. The shelf width is ≤12 km west and ≤18 km east of the canyon area, respectively, but is as narrow as 1 km in the canyon area, where shallow channels dissect modern reef structures.

A few Holocene and Plio-Pleistocene faults have been mapped on shore in the vicinity of the 2019-2020 SWPR seismic swarm. Mid-Holocene faults were trenched in Lajas Valley (*Prentice and Mann*, 2005) and near Ponce (*Piety et al.*, 2018). A fault, named San Francisco Fault, which can be extrapolated into Guyanilla Bay was suggested by Grossman (1963) from surface geology. A 33-km-long left-lateral strike-slip fault, named Punta Montalva Fault, stretching from Punta Montalva to north Boquerón Bay on the west coast of Puerto Rico was postulated largely based on morphology by Roig-Silva et al. (2013) (Fig. 3). Garrison (1969) interpreted a several-hundred-milliseconds-deep half graben in Sparker seismic reflection data on the insular shelf south of Ponce. The graben is bounded by the Caja de Muertos Fault on the SE and possibly the Bajo Tasmanian Fault on the NW (Fig. 2). Caja De Muertos Island was proposed to have been uplifted by faulting during the Miocene or later (*Kaye*, 1957). The area of seismic activity is largely devoid of good quality seismic reflection data.

3. Data and Methods

We conducted a high-resolution multichannel seismic survey between March 7-13, 2020 aboard the University of Puerto Rico's R/V Sultana based at the Marine Sciences laboratory at Magueyes Island in La Parguera (Figs. 2 and 4). The seismic sources included a 2.4 kJ Sparker at water depths >500 m, a 1 kJ Sparker at water depths of 100-500 m and a 0.3 kJ mini-sparker on the 8-25 m deep shelf. Acoustic data was received by a 32-channel digital streamer with hydrophone group interval of 1.5625 m. Navigation was carried out by a Hemisphere R131 Differential and WAAS (Wide Angle Augmentation System) enabled GPS receiver with horizontal accuracy of 2-3 m (*Baldwin et al.*, 2021). A total of 250-line km were collected with common mid-point (CMP) spacing of 0.781 m for lines on the shelf and 3.125 m for lines on the insular slope. The vertical resolution is estimated at a few meters. Data processing included geometry definition, trace edits, static correction, noise reduction (f-k deconvolution, f-k filtering, bandpass filtering (70-1000 Hz), CMP stack, post-stack phase-shift time migration, and spiking deconvolution. Horizon and fault interpretation and visualization were carried out with Kingdom Suite© software. Data penetration was typically ≤ 0.5 s (~500 m) on the slope and ≤0.08 s on the shelf (Fig. 4). Deeper penetration on the shelf was masked by multiples due to the shallow and sometimes hard modern reef bottom.

Multibeam bathymetry data, collected by the NOAA ships Nancy Foster and Thomas Jefferson prior to 2019, and LIDAR data, collected by NOAA on the shelf (see Appendix A4 for data sources), were gridded at 8 m horizontal resolution. We added these data to an existing compilation of multibeam bathymetry data in the NE Caribbean (*Andrews et al.*, 2014).

On land we used Synthetic Aperture Radar interferometry (InSAR) measurements of displacements in the radar line-of-sight directions and combined data from different directions to estimate two components of the surface displacement. InSAR measurements from satellites in this region are sensitive to the east and vertical components. The data included C-band (5.6 cm wavelength) SAR from the Copernicus Sentinel-1 satellites, operated by the European Space Agency (ESA), and L-band (24 cm wavelength) SAR from the Japan Aerospace Exploration Agency (JAXA) Advanced Land Observation Satellite-2 (ALOS-2) satellite. Two tracks of Sentinel-1 data cover the land area of the seismic activity, and another track covers the area to the east. SAR and InSAR processing were done with the InSAR Scientific Computing Environment (ISCE) v2 (*Rosen et al.,* 2012) starting with the single-look complex images from ESA and

JAXA. Stack processing was performed with ISCE on two of the Sentinel-1 tracks descending track D098 and ascending track A135, for all data from July 2019 through early August 2020. Time-series analysis was conducted with MintPy (*Yunjun et al.,* 2019) to reconstruct the line-of-sight displacements for all the dates on each track and to estimate the coseismic step functions at the times of the Mw 6.4 January 7, 2020 earthquake and the events around July 3, 2020 and better separate the earthquake deformation from atmospheric effects (*Fielding et al.,* 2017). We processed wide-swath (ScanSAR) data from ALOS-2 to form a coseismic interferogram on descending path 135 using the ALOS-2 application in ISCE2 (*Liang and Fielding,* 2017).

We combined line-of-sight (LOS) displacement estimates from the step-function fits to the Copernicus Sentinel-1 time series. The LOS (ground-to-satellite vector) for the Sentinel-1 ascending track A135 is up and slightly north of due west, while the LOS for the descending track D098 is up and slightly north of due east. We used the same reference point at 18.0°N and 67.0°W for both tracks. The displacements are set to zero at the reference point, and all the other displacements are given relative to this point. We can combine the two InSAR LOS measurements to estimate two components of the surface displacements that are close to east and vertical but contain a small percentage of any north displacement (*Wright et al.,* 2004). The resulting estimates for the vertical and east components of coseismic displacements were contoured. The estimated vertical component of coseismic displacements due to the Mw6.4 January 7, 2020 is the difference between the time-series step-function at the interval between 01/02 -01/14/2020 and are shown as red contours on Fig. 5. The horizontal component is smaller than the vertical and is not shown.

We did a similar step-function fit to the two Sentinel-1 time series for July 3, 2020. As with the January step-function fit, the 12-day intervals between acquisitions on the two Sentinel-1 tracks means that all deformation in the time between acquisitions cannot be separated. For the A135 track, the interval that contains July 3 was 07/02–07/14 and for the D098 track the interval was 06/30–07/12. The conversion to vertical and east components assumes that the surface displacements are the same in the two step-function fits, which should be accurate if nearly all the displacement was between 07/02 and 07/12. This interval includes several earthquakes, the largest were a pair of Mw4.9 and 5.3 on 07/03. The estimated vertical component is shown on Fig. 6. An area of coastal subsidence that is much smaller than the Mw 6.4 signal was detected near Playa Santa that may be due to one of the Mw4.9 or the Mw5.3 07/03 earthquakes offshore (Fig. 6). The subsidence was accompanied by westward horizontal component west of Playa Santa and an eastward component east of Playa Santa.

GPS time series relative to the Caribbean reference frame for 9 stations surrounding the study area (Fig. 1) were downloaded from the Nevada Geodetic Laboratory (*Blewitt et al.,* 2018). We used the data that was processed with the final GPS orbits. The time series were used to evaluate relative plate motions within the region and encompassed available continuous observations for at least 4 years since 2008 and prior to the start of the seismic sequence.

Locations and focal plane solutions of Mw≥4.5 earthquakes in this sequence, published by the Advanced National Seismic System (ANSS) Comprehensive Earthquake Catalog (ComCat) (https://earthquake.usgs.gov/earthquakes/search/ accessed February 15, 2021) have been adopted for analysis here.

The epicenter of small earthquakes in Fig. 2 were relocated using the HypoDD algorithm (*Waldhauser & Ellsworth,* 2000) using the Puerto Rico Seismic Network (PRSN) P and S arrival pick data between 12/15/2019-08/19/2020. The parameters applied in the relocation were as follows: maximum separation distance of 7 km, minimum observations per event 16, minimum number of pairs 12. With these constraints, 7130 earthquakes were retained for relocation (*Vanacore et al.,* 2021).

4. Observations and modeling

4.1 Seismic reflection

Faulting was interpreted in the seismic profiles where continuous reflectors were offset by discontinuities and diffractions. Faults were typically characterized by zones of opaque reflectivity extending sub-vertically for a few hundreds of milliseconds (Fig. 4). The observed faults typically do not offset the sea floor but end a few tens of milliseconds below it. The faults we mapped are concentrated in three specific areas. Most of them are distributed 3.5-7 km seaward of the shelf edge between Guayanilla and Guanica (Figs. 2 and 4). Two additional fault groups were identified, one on the slope SW of Ponce Basin (Fig. 4f, g and h), and the second group at distances of 17-21 km from the shelf edge. Fault zones were not identified elsewhere in the survey area, i.e., closer to the shelf edge or in the zone between 7 and 17 km from the shelf edge. Apparent dips of the mapped fault zones range from ~45° to sub-vertical.

The insular shelf platform is typically < 20 m deep, is rimmed by modern fringing reefs at the shelf edge mantled by patch reefs, cays and pavement-encrusted coralline algae, stony corals

(Scleractinia) and sponges (*Ballantine et al.,* 2008). The cays and shallow shoals were often hazard to navigation and interfered with data acquisition.

Seismic profiles collected on the shelf were of low-quality relative to offshore profiles due to greater noise and limited penetration of the seismic energy. Accordingly, it was challenging to distinguish between folds, the irregular boundaries separating reefs from adjacent inter-reef sediment-filled depressions, and offsets or disturbances of horizontal reflectors that may be indicative of faults. However, sub-vertical fault traces were identified in a few locations (Fig. 4). Faults were interpreted in two parallel seismic lines offshore Punta Montalva, one in the vicinity of the offshore continuation of Punta Montalva Fault, and a second farther south (Figs. 2 and 4c). Faults were also identified on the shelf within (Fig. 4e) and seaward of Guayanilla Bay, as well as south of Playa Santa and La Parguera.

4.2 Surface subsidence and displacement

Eyewitnesses reported permanent flooding of parts of El Faro (Fig. 5), a coastal community in Guayanilla, immediately following the Mw6.4 event (C. von Hillebrandt-Andrade, NOAA, , Written Comm., 2020; *Pérez-Valentín et al.,* 2021). Permanent flooding was also documented in other coastal locations in surveys conducted during the week following the earthquake (green dots in Fig. 5; *Allstadt et al.,* 2020). Subsidence during the time interval of 01/02-01/14/2020 with a maximum of 20 cm was observed InSAR time-series and based on the eye-witness reports was assumed to be due to the Mw6.4 January 7, 2020 (Fig. 5). The long axis of the subsidence was oriented in a NE-SW- direction with amplitude increasing offshore. We forward modeled vertical subsidence with Coulomb 3.3 software (*Toda et al.,* 2010) assuming an elastic half space and using the focal plane parameters for the Mw6.4 earthquake reported by the ANSS-ComCat (strike, dip, rake, and seismic moment of 268°, 43°, -58°, and 5.04e18 N-m, respectively). The fit of the model to the shape of the observed subsidence anomaly was significantly improved when a rake of -72° was used instead of -58° (i.e., a relatively larger normal component and smaller left-lateral component than the ANSS solution). Trial-and-error modeling of the rupture length, width, and slip, which conform to the seismic moment provided by ANSS-ComCat, resulted in the best fitting model of top and bottom depths of 2 and 10 km, rupture length of 11.3 km, and a uniform slip of 1.265 m. These values are close to those of Liu et al. (2020) who estimated peak slip of 1.6 m and main slip patch between 3-13 km from kinematic inversion of GPS and strong motion data. Our model used the typical crustal shear modulus of μ = 30 GPa. Our best-fit model predicts a maximum subsidence of 0.45 cm offshore centered at the upper reach of Guayanilla Canyon (Fig. 5).

The location of our modeled fault plane (rectangle in Fig. 5) and its dip also match the relocated micro-seismicity by Vanacore et al., (2021) from 01/07-08/2021 (the rupture day and the following day) (Inset in Fig. 5). Micro-seismicity on 01/07/2020 prior to the Mw6.4 earthquake was limited to depths <8.5 km but extended downward to ~15 km after the event, suggesting that the rupture continued to propagate deeper.

The ANSS-ComCat preferred earthquake epicenter falls, however, outside the surface projection of the fault plane (Fig. 5), but an alternate epicenter determined by the PRSN and listed in the ANSS-ComCat (17.9578°N, 66.8113°W, Table A1) is located near the bottom edge of the modeled slip patch (Star in Fig. 5 and in inset). Similarly, the PRSN alternate epicenter of the 01/06/20 Mw5.8 earthquake, which was thought to trigger the Mw6.4 earthquake is located within the modeled fault patch, whereas the preferred ANSS-ComCat location is 5 km to the south.

A second much smaller coastal subsidence (≤ 0.04 m) was detected near Playa Santa from the InSAR time-series fit for the period between 07/02-07/12/2020 (red contours in Fig. 6). Two offshore moderate-size earthquakes occurred during this period, a Mw5.3 07/03 (primarily left-lateral strike-slip) and a Mw4.9 07/03 (primarily normal) closer to shore. The subsidence was accompanied by horizontal displacement with opposing directions west and east of Playa Santa and a maximum amplitude of 8 cm. However, the InSAR anomaly cannot distinguish between east and north displacements, because the satellite lines-of-sight in this area are primarily east and west. Additionally, GPS data from station PRMI (Nevada Geodetic Laboratory, *Blewitt et al.*, 2018; Fig. 1) document a step change in the horizontal displacement components around 07/03/2020 with the north component being almost double the east component. We therefore limited our modeling to the InSAR subsidence anomaly. The vertical subsidence was modeled with Coulomb 3.3 software (*Toda et al.,* 2010) using the focal parameters published in the ANSS-ComCat for both the Mw5.3 and Mw4.9 that occurred during the observation period (Table A3). Because the preferred focal plane parameters in the catalog produced significant misfits to the observations, we tested the alternate focal plane parameters provided in the catalog varying only the top and bottom depths of the fault, its average slip, and its location. The model that best fits the observed subsidence is shown in Fig. 6. It uses the alternate focal plane parameters for the Mw5.3, and the fault plane is shallow (0.5-3.5 km). The shallow depth is compatible with the origin depth in the ANSS-ComCat (3 km) but the modeled fault plane is located closer to shore than the published epicenter (Fig. 6). The mixed left-lateral and normal motion (rake of -27°) of the best-fit subsidence model may indicate that the Punta Jorobado peninsula (Fig. 6) has formed as a result of recurring earthquakes with a similar sense of motion.

5. Interpretation

5.1 Seismic reflectors

Seismic reflection profiles crossing the insular slope show patches of surficial sediment cover spanning ≤0.05 s two-way travel time (< 50 m assuming seismic velocity < 2000 m/s) except where deposited in depressions on the flanks of canyon interfluves (Fig. 4). The underlying reflectors are discontinuous, either because of poor acoustic penetration or due to collapse and tilting of small blocks, the latter being observed on shore (*Monroe*, 1980; Renken et al., 2002; *Mann et al.*, 2005). The ages of these reflectors cannot be verified without borehole data.

Tilted seismic reflectors were observed to increase in thickness toward the south in the vicinity of the headwater of the Guayanilla Canyon (e.g., Fig. 4d), which may represent an asymmetric depocenter. This depocenter is located in the region of maximum subsidence from modeling the InSAR data (Fig. 5). The density and orientation of the seismic profiles do not allow us to map the extent of the region of tilted reflectors with confidence. The internal stratigraphy of the tilted reflector geometry is discontinuous and does not allow us to determine if the reflectors fan out representing constant sediment supply to the depocenter during tilting and subsidence. It is also possible that sediment supply does not keep up with subsidence and/or the sediments are being transported to deeper water.

5.2 Associating mapped faults with seismic events and fault planes

Fault parameters such as dip, strike, and rake cannot be deduced from the profiles, because of the sparse line distribution and because shallow deformation in relatively poorly consolidated sediments is often not indicative of fault parameters at depth (e.g., *Harding,* 1985; *Withjack et al.*, 1995). The lack of sea floor offset typically associated with sub-vertical faults interpreted in the seismic profiles either indicates that these fault zones have not been active during the most recent seismic activity or that the shallow sub-seafloor sediments are unconsolidated and do not deform in a brittle fashion (e.g., *Kaneko and Fialko*, 2011). In places, we do observe shallow sediments that consist of landslide debris unconformably overlying the deeper sediments, which supports the latter hypothesis.

We can try to associate the locations of observed faults with specific clusters of earthquakes and with fault planes derived from the InSAR data. The spatial distribution of the mapped faults, mostly close to the shelf edge, and rarely or not in deeper water, is similar to the spatial distribution of the 2020 seismic sequence, suggesting that earthquake activity in the region has in the recent geologic past been probably limited to the nearshore area in the recent geologic past. More specifically, the belt of observed faults 3-7 km south of the shelf edge in the seismic data could correspond to the shallow strain relief associated with the Mw6.4 rupture (blue rectangle in Fig. 2b) and/or the rupture of other earthquakes before and after this earthquake (Figs. 2a and 2b). The faults on the shelf south of Guayanilla Bay may all be pre-existing, but also could have been reactivated during the 01/07/2020 Mw6.4 earthquake or the 01/20/2020 earthquake cluster (green in Fig. 2c). The fault in the middle of Guayanilla Bay (Figs. 2c and 4e) may be the extension of one of the faults crossing the bay from west to east (*Grossman,* 1963; J. Joyce, Written Comm., 2020). A better delineation of this fault is needed because of its location under a population center and critical industrial facilities.

However, the association of other observed faults in the seismic reflection data with the locations of moderate or large earthquakes is less straight forward. Several faults were observed SW of Caja de Muertos Fault and Ponce Basin, but moderate-size seismic activity did not extend to that area (Fig. 2). Whether this area is still seismically active, is unknown. One possibility is that these no longer active faults undergo shallow creep induced by nearby large earthquakes existing faults. An example of such phenomenon (although on an active fault) is the observed shallow creep deformation on the Garlock Fault, California, following the Ridgecrest earthquake 5-20 km away (*Ross et al.*, 2019).

5.3 The role of Punta Montalva Fault in the seismic sequence

The Punta Montalva Fault was proposed by Roig-Silva et al. (2013) to be an active strike-slip fault extending for 33 km from the tip of Punta Montalva northwestward to Boqueron Bay (Fig. 3) This proposed fault appears, however, to have had a little role in the initiation of the 2019-2020 seismic sequence, which started several km ENE of the southeastern end of the fault (Fig. 2a). Only during June 2020, five months after the 01/07/20-2020 Mw6.4 earthquake, did moderate-sized strike-slip earthquakes take place onshore along the southeastern-most 5-km of the fault (Fig. 2d). Adames-Corraliza (2017) considered this 5-km-long onshore fault segment to be active based on offset measurements made from LIDAR and Ground Penetrating Radar data. The majority of the proposed fault to the northward was not associated with either moderate or micro seismicity during the 2019-2020 seismic sequence (Fig. 2). The role of the Punta Montalva fault in accommodating the differential block model in SWPR, therefore remains unknown. An evaluation of the potential seismic activity along the entire 33-km-long strike-slip fault is important because rupture of the entire length can generate an M6.9 earthquake (*Wells and Coppersmith*, 1994).

5.4 Progression of seismic activity

Moderate-size (≥ Mw4.5) earthquake activity shows a complex temporal development of both strike-slip and normal faults. Fig. 2 shows our interpreted color-coded clusters with their temporal progression following the color spectrum from purple to red (inset in Fig. 2a). Epicenters of small earthquakes relocated using the HypoDD algorithm (*Vanacore et al.,* 2021) that took place during most of the dates of moderate-size earthquake activity were plotted with colors similar to their respective moderate-size earthquakes. Their distribution provides the spatial context to the ruptures associated moderate-size earthquake activity.

Earthquake activity started SE of Guayanilla on 12/28/2019 and advanced to the SE along one or more faults by Mw ≤5 earthquake having left-lateral strike-slip focal mechanisms (Fig. 2a). This activity triggered an Mw5.8 strike-slip earthquake on 01/06/2020, which was located within the patch of the 01/07/2020 Mw6.4 fault plane modeled from the InSAR subsidence. The Mw6.4 in the early morning of 01/07/2020 occurred within this patch and additional normal and strike-slip ruptures extended SE and north of the patch, perhaps along secondary faults (Fig. 2b). Normal and strike-slip fault ruptures, including an Mw5.9 earthquake, took place along the western side of the Mw6.4 patch 3-7 days later (1/10-1/14/20) and were accompanied by intense micro-seismicity along a 20-km-long NNE-SSW-oriented belt (blue dots in Fig. 2c). However, the locations and focal mechanisms of moderate earthquakes during this period suggest that this belt of seismicity is not a single fault. Normal fault ruptures on 1/20/20 (green in Fig. 2c) and east of it on 05/02/20 (yellow in Fig. 2d) took place along the eastern edge of the Mw6.4 rupture plane. Left-lateral strike-slip earthquakes took place along the NE and western edges of the patch on 08/07/20 (brown in Fig. 2d) and 12/24/20 (dark grey in Fig. 2d). Seismic activity intensified 10-15 km west of the Mw6.4 rupture plane during June-July 2020 with some events probably occurring along the SE section of Punta Montalva Fault (orange in Fig. 2d) and others under the shelf (red in Fig. 2d). The latter events were probably associated with the small coastal subsidence and horizontal motion, detected by InSAR, which was discussed in section 4.2 and Figure 6.

Several inferences can be drawn from this sequence of events: First, the sequence is not a typical foreshock-mainshock-aftershock sequence. We base this inference on two lines of evidence: (a) The magnitudes of the seismic sequence did not follow Båth's Law. Båth's Law states the largest aftershock is 1-1.2 magnitude levels smaller than the main shock (e.g., *Shcherbakov and Turcotte,* 2004). (b) The energy released during the 01/07/2020 Mw6.4 earthquake was only 64% of the total energy released during the seismic sequence, assuming similar stress drop during all the earthquakes. Second, the area may be crisscrossed by intersecting network of short faults, which were probably activated by the changing stress field caused by the progression of rupture along different faults. Third, the earthquake sequence was probably initiated by offshore strikes-slip fault(s) SE of Guánica (Fig. 2a), and not by rupture on the Punta Montalva Fault as initially proposed (*López-Venegas et al.*, 2020). Moderate earthquakes on the Punta Montalva Fault occurred only during June-July 2020.

6. Discussion

6.1 Longer term tectonic activity

Several lines of evidence indicate that the seismic sequence in SWPR is but the latest episode of a repetitive earthquake cycle, whose recurrence interval is unknown. The extension directions indicated by the T-axis analysis of moderate (M≥4.5) earthquakes from the ANSS-ComCat (329°±10°; heavy double-sided arrows in Fig. 7, Table A1) are similar to those derived by Mann et al. (2005) from the study of terrestrial fault striations in the area (303°-344°) (double-sided blue arrows in Fig. 7). The age of the terrestrial faults is estimated at post-early Pliocene based on cross-cutting relationships with older faults (*Mann et al.,* 2005).

The area of seismic activity is the only part of southern Puerto Rico where the shelf is indented northward, and the shelf edge becomes as narrow as 1 km (Fig. 7). The subsidence model for the 01/07/2020 Mw6.4 earthquake predicts the location of maximum subsidence to be at the headwaters of this canyon (white star in Fig. 7), and recurrent rupture of this fault could have helped create the shelf indentation in this area.

We interpret the tilted geometry of the sedimentary fill (Fig. 4d) to be the result of an episodic rupture of a normal fault(s), which progressively down throws the north side of the fault(s) and traps sediments into an asymmetric depocenter. The observed thickness of the depocenter, at least 0.5 sec (~500 m), suggests that the depocenter had developed over a significant time period. The depocenter is collocated with region of maximum subsidence due to the Mw6.4 earthquake, modeled from the InSAR data. The recurrence interval of earthquakes similar to the Mw6.4

earthquake is unknown, but if its average slip (1.27 m) is representative, then the depocenter developed over hundreds of earthquake cycles.

The bathymetry also shows two NE-oriented bathymetric lineaments that are deeper to the NW despite the general southward dip of the insular slope (dashed blue lines in Fig. 7). These lineaments, and the down-to-the-NW normal displacement of many of the earthquakes' focal mechanisms, including the largest Mw6.4 event, suggest relative subsidence close to shore and relative uplift farther away from shore toward the SE.

The area of seismic activity is located at the headwaters of the only large submarine canyon along southern Puerto Rico, the Guayanilla Canyon. Given the lack of major terrestrial rivers feeding the canyon system, the canyon system has likely developed to evacuate the sediments of the collapsing shelf edge by repeated normal faulting. The canyon system itself might have been partially affected by the repeated seismic activity, as is evident by the curious right-angle meandering of the eastmost tributary of the canyon. These abrupt meanders may be controlled by subsurface faults (dashed blue lines in Fig. 7). Since submarine morphology typically develops over a long geological time, the presence of the shelf indentation, unique lineaments and meanders are other indicators for a long-term history of seismic activity.

6.2 Diffuse tectonic boundary

The convergence rate and azimuth of the North American Plate with the Caribbean Plate are relatively constant across the span of the 800 km of the Puerto Rico Trench with deviations arising only from local variability in plate boundary orientation (Fig. 1). Nevertheless, seismic coupling appears to vary significantly across the plate boundary. The sector from the longitude of Mona Rift westward (Henceforth, Hispaniola) is associated with several large 20th century earthquakes (e.g., *ten Brink et al.*, 2011), with partitioning of the GPS motion between sub-perpendicular convergence and sub-parallel strike slip, and with the accumulation of large strains on the upper plate (*Symithe et al.*, 2015). The sector east of the longitude of Mona Passage (henceforth, Puerto Rico) is associated with smaller earthquakes, many of them showing oblique slip sub-parallel to the convergence direction (*ten Brink*, 2005; *ten Brink et al.*, 2011). GPS velocities in Puerto Rico relative to the Caribbean plate are 1/5 those in Hispaniola, likely because of significant differences in coupling across the subduction interface between the Puerto Rico and Hispaniola segments of the trench (Fig. 1) (*ten Brink and López-Venegas*, 2012; *Symithe et al.*, 2015).

The difference in azimuth and magnitude of the GPS velocity between Puerto Rico and Hispaniola suggests the presence of a boundary between the upper plate blocks of Hispaniola and Puerto Rico. This boundary crosses the island arc, but its location and nature are poorly defined. GPS block models provide a relative block motion estimate of 1-5 mm/y (e.g., *Symithe et al.*, 2015). Mann et al. (2002), Manaker et al. (2008), and others suggested that the boundary connects Mona Rift to Yuma Basin. Detailed multibeam bathymetry and seismic reflection mapping show a system of WNW-ESE normal faults with a nested fault-system oriented NW-SE exposed at the sea floor, which presumably indicates neo-tectonic NE-SW motion across the boundary (*Chaytor and ten Brink*, 2010). Ten Brink and López-Venegas (2012) using GPS measurements between 2008-2011 noted that stations PRMI in SWPR and MOPR on Mona Island (see Fig. 1 for location) move in the direction of Hispaniola whereas stations farther to the north and to the east move with the direction of the Puerto Rico block. They also noted a seismicity belt extending from Mona Rift to the SE through southwest PR. Solares-Colon (2019) used the F-test to support the independent motion of SWPR recorded by GPS with respect to the Puerto Rico block, and its similar direction to Mona Island and eastern Hispaniola. The width of the accretionary wedge of Muertos Trough changes significantly at the longitude of the SW corner of PR (*Granja-Bruña et al.,* 2009). The change in the width of the accretionary prism may correspond to the location of the block boundary, assuming that the Muertos accretionary prism is a back-arc wedge of the Puerto Rico-Hispaniola subduction zone (*ten Brink et al.,* 2009).

Elastic strain commonly accumulates in the locked parts of the subduction interface during inter-seismic times dragging the overlying arc in the direction of subduction at a significant fraction of the subducting plate velocity (Fig. 8b). GPS velocities in Hispaniola show a southwestward azimuth sub-parallel to and at a significant fraction to the incoming North American plate. GPS velocities in Puerto Rico and the Virgin Islands, are in contrast, significantly slower than the incoming plate velocity and are oriented WNW, i.e., their north component is opposite to the subduction direction (Fig. 1). The GPS velocities in Puerto Rico and the Virgin Islands were interpreted to indicate very low coupling across the subduction interface north of these islands and their tilting into the trench (*ten Brink*, 2005: *ten Brink and López-Venegas*, 2012). We propose that the Western Puerto Rico Deformation Boundary (Fig. 1) is driven by variations in seismic coupling on the Puerto Rico subduction interface, with high coupling north of Hispaniola and Mona passage and almost no coupling north of Puerto Rico (*Symithe et al.,* 2015). The deformation boundary may have several deformation domains: Mona rift in the north is a classical rift graben bounded by a fault on its east side and perhaps another one on its west side.

Mona Passage farther south exhibits NW-SE series of faults, many of them not organized in a uniform fashion (*Chaytor and ten Brink*, 2010). Some of these faults may extend eastward on land (*Grindlay et al.*, 2005). SWPR is characterized by subdued topography and east-west valleys (e.g., Lajas Valley) and faults *(Prentice and Mann, 2005).* The recent seismic activity, reported here, describes a NW-SE extension offshore SWPR. It may connect to the Muertos back-arc accretionary wedge, which is significantly wider west of the deformation boundary.

We suggest that the Western Puerto Rico Deformation Boundary is similar to a diffuse zone of deformation observed in the Middle America arc (*Marshall et al.*, 2000), Marshall et al. (2000) suggested that a change in coupling at the subduction interface is associated with a change from a smooth subducting seafloor offshore Nicaragua and northwestern Costa Rica to a rough seafloor in southeastern Costa Rica and Panama (Fig. 8a). This lateral change in coupling, they hypothesized, causes differential movement of the arc with respect to the interior Caribbean plate, which is accommodated by a diffuse region of deformation, named Central Costa Rica Deformation Boundary (*Marshall et al*, 2000). It also affects the development of a back-arc accretionary wedge north of southeastern Costa Rica and Panama, known as the Northern Panama Deformation Belt (NPDB), which overthrusts the Caribbean plate. The Central Costa Rica Deformation Boundary exhibits several faulting domains with different faulting styles, recurring cycles of small and moderate earthquakes, and a change in the magnitude and orientation of the GPS velocity vectors from the Caribbean plate across the zone of diffuse deformation and to the Panama Block. Some of the seismic cycles in the deformation boundary have been triggered by large subduction or back-arc earthquakes.

Similar elements can be found along the Puerto Rico-Hispaniola inactive arc. Coupling of the subduction interface north of Puerto Rico appears low whereas west of Mona Rift and along the Hispaniola sector of the trench, coupling is high (e.g., *Symithe et al.*, 2015). The collision of the thick crust of the Bahamas Bank with the subduction zone north of Hispaniola may play a major role in the high seismic coupling along this sector. Differential coupling across the subduction zone creates an irregular boundary across the volcanic arc, which exhibits diffuse deformation. Muertos thrust belt is well developed south of Hispaniola and is poorly developed south of Puerto Rico (Fig. 1; *ten Brink et al*., 2009) similar to the NPDB north of the rough seafloor of southeastern Costa Rica and Panama.

Alternatively, the seismic sequence of SWPR may perhaps be explained in the context of a slight north-south extension across the island arc in Puerto Rico, driven by strong coupling between the arc and the interior Caribbean plate and a weak coupling of the arc across the subduction zone to the north (Fig. 9) leading to tilting and collapse of the forearc (*ten Brink*, 2005). Extension in the southern part of the arc is evident by the basin morphology of Virgin Island Basin and Whiting Basin SE of Puerto Rico, and the possible extension across a narrow elongate bathymetric ledge at the upper slope south of the island south of Puerto Rico (Fig. 7), sometimes named Investigator Fault (e.g., *Mann et al.*, 2005). SWPR also has a unique valley and range-like topography, indicating a relative north-south extension. The continuous pre-2020 high-resolution terrestrial GPS data (Table A2) also appear to indicate opposing roughly N-S motion between pairs of stations across the two blocks in question (Fig. 9b).

6.3 Why doesn't the deformation zone mature?

The recent seismic activity shows that despite being subjected to this tectonic/structural regime since perhaps post Early Pliocene, deformation continues to be accommodated along many small faults and has not coalesced into a mature boundary. We can offer several hypotheses to explain this observation. First, the rate of deformation at this boundary is low, perhaps 1-2 mm/y (1-2 km per Ma), and therefore, the coalescence of many faults into one or a couple of major faults may take a lot longer in the NE Caribbean. A second and perhaps more plausible hypothesis is that the inherited island arc structure and composition, such as in Puerto Rico (Fig. 3) are anisotropic because the accretion process that built these arcs is fundamentally two dimensional. The anisotropic composition of the arc may promote long along-arc faults, such as strike-slip faults in oblique convergence regimes, and short faults with chaotic orientations at block boundaries across the arc. For example, Styron et al. (2011) show that oblique convergence in the Himalaya results in long arc parallel strike-slip faults (e.g., Karakorum Fault) and much shorter arc perpendicular normal faults (e.g., Tibrikot Fault). Mapped cross-arc faults in Central Costa Rica Deformation Boundary, seldom span more than 20 km (Table 1 in *Marshall et al.,* 2000).

7. Conclusions

The 2019-2020 southwestern Puerto Rico (SWPR) seismic sequence ruptured multiple short normal and strike-slip faults along the insular shelf and upper slope of southwest Puerto Rico. The seismic activity included many moderate-size earthquakes over a span of a year and did not follow a typical main shock-aftershock sequence. InSAR-detected coastal subsidence, earthquakes clustered in time and space, and sub-seafloor faults, detected in high-resolution seismic reflection survey, attest to the existence of multiple rupturing faults at different orientations. Despite morphological and structural indicators of a long-term deformation history of similar nature, the deformation does not seem to center on one or more mature fault, perhaps because of the heterogenous composition and structure across the arc. The 2019-2020 seismic sequence may be the southernmost domain of a diffuse deformation boundary between the Hispaniola and Puerto Rico blocks, which also includes the domains of SWPR, eastern Mona Passage, and Mona Rift. The diffuse zone, which we name the Western Puerto Rico Deformation Boundary may be analogous to the Central Costa Rica Deformation Boundary and may be driven by variations in subduction coupling along the Puerto Rico Trench.

Acknowledgements and Data

The logistical support of the University of Puerto Rico Department of Marine Sciences in carrying out a rapid response seismic reflection survey only two months after the largest earthquake in the sequence is greatly appreciated. The logistical support included the use of the R/V Sultana and shore support at the department’s shore lab in Isla Magueyes at no cost. We thank Prof. Ernesto Otero, director, and Aldo Acosta, communication specialist, and Captain Orlando Espinoza and his crew for all their generous help. Christa von Hillebrandt, and Victor Huérfano helped facilitate logistical issues. This work contains modified Copernicus data from the Sentinel-1A and -1B satellites provided by the European Space Agency (ESA). Original ALOS-2 data and products are copyright JAXA and provided under JAXA ALOS Research Announcement 6 (RA6). Part of this research was performed at the Jet Propulsion Laboratory, California Institute of Technology under contract with the National Aeronautics and Space Administration and supported by the Earth Surface and Interior focus area. We thank Robert Herrmann and Jessica Murray for helpful discussions and Kate Allstadt and Claudia Flores, USGS, for thorough and helpful reviews. Detailed and thoughtful comments by Tectonics

Associate Editor Laura Giambiagi and by John Weber and an anonymous reviewer helped improve the manuscript. Any use of trade, firm, or product names is for descriptive purposes only and does not imply endorsement by the U.S. Government.

Seismic reflection data and navigation can be downloaded from https://www.sciencebase.gov/catalog/item/60a2d193d34ea221ce432fe5. Earthquake data can be found in ANSS-ComCat https://earthquake.usgs.gov/earthquakes/search/. Supplemental Table A1 lists the catalog parameters of earthquakes with Mw ≥ 4.5 including alternative locations, plotted in Fig. 2. GPS data can be found at http://geodesy.unr.edu/magnet.php. Supplemental Table A2 lists the parameters of the stations appearing in Fig. 1. Processed InSAR data can be found in https://aria-share.jpl.nasa.gov/20200106-Puerto_Rico_EQ/Displacements/. Original Copernicus Sentinel-1 data is available at no charge from the Copernicus Sentinels Scientific Data Hub (https://scihub.copernicus.eu/) and is mirrored at the NASA Alaska Satellite Facility archive center https://search.asf.alaska.edu/. Original ALOS-2 data is available from JAXA (https://auig2.jaxa.jp/ips/home). Bathymetry data can be found in https://doi.org/10.25921/ds9v-ky35 and Andrews et al. (2014). For further details see Appendix A4.

References

Adames-Corraliza, Á. R. (2017). Geomorphic and geophysical characterization of the north Boquerón Bay-Punta Montalva fault zone: A capable fault system in southwestern Puerto Rico, M.Sc. thesis, 147 pp., Univ. Puerto Rico, Mayaguez.

Allstadt, K.E., Thompson, E.M., Bayouth García, D., Irizarry Brugman, E., Hernandez, J.L., Schmitt, R.G., Hughes, K.S., Fuentes, Z., Martinez, S.N., Cerovski-Darriau, C., Perkins, J.P., Grant, A.R., and Slaughter, S.L., 2020, Field observations of ground failure triggered by the 2020 Puerto Rico earthquake sequence: U.S. Geological Survey data release, https://doi.org/10.5066/P96QNFMB.

Andrews, B.D., U.S. ten Brink, W.W. Danforth, J.D. Chaytor, J-L Granja-Bruna, P. Llanes Estrada, and A. Carbo-Gorosobel (2014) Bathymetric terrain model of the Puerto Rico Trench and Northeast Caribbean for marine geological investigations, USGS OFR 2013-1125.

Baldwin, W.E., Chaytor, J.D., Foster, D.S., Moore, E.M., Nichols, A.R., and ten Brink, U.S., 2021, Multichannel seismic-reflection and navigation data collected using SIG ELC1200 and Applied Acoustics Delta Sparkers and Geometrics GeoEel Digital Streamers during U.S. Geological Survey Field Activity 2020-014-FA, southwest of Puerto Rico, March 2020: U.S. Geological Survey data release, https://doi.org/10.5066/P96GY6TQ.

Ballantine, D. L., R. S. Appeldoorn, P. Yoshioka, E. Weil, R. Armstrong, J.R. Garcia, ... and C. Lilyestrom (2008). Biology and ecology of Puerto Rican coral reefs. In *Coral Reefs of the USA*, pp. 375-406. Springer, Dordrecht

Blewitt, G., W. C. Hammond, and C. Kreemer (2018), Harnessing the GPS data explosion for interdisciplinary science, *Eos*, **99**, https://doi.org/10.1029/2018EO104623

Chaytor, J.D., and U.S. ten Brink (2010). Extension in Mona Passage, Northeast Caribbean, *Tectonophys.* **493** 74-92.

Dascher-Cousineau, K., Lay, T., & Brodsky, E. E. (2020). Two foreshock sequences post Gulia and Wiemer (2019). *Seismol. Soc. Am.* **91** 2843-2850.

DeMets, C., Jansma, P.E., Mattioli, G.S., Dixon, T.H., Farina, F., Bilham, R., Calais, E., Mann, P. (2000). GPS geodetic constraints on Caribbean-North America plate motion. *Geophys. Res. Lett.,* **27** 437–440.

Fielding, E. J., S. S. Sangha, D. P. S. Bekaert, S. V. Samsonov, and J. C. Chang (2017). Surface Deformation of North-Central Oklahoma Related to the 2016 Mw 5.8 Pawnee Earthquake from SAR Interferometry Time Series, *Seism. Res. Lett.* **88** 971-982.

Fielding, E.J., E. Vanacore, and A. López-Venegas (2020) SAR imaging of the coseismic and postseismic deformation from the 2020 southwest Puerto Rico seismic sequence, Geo. Soc. Am. Annual meeting 2020, presentation 139-4.

Garrison, L. E. (1969) Structural geology of the Muertos insular shelf, Puerto Rico US Geological Survey OFR 69-103.

GEBCO Compilation Group. (2020). GEBCO 2020 grid https://doi.org/10.5285/a29c5465-b138-234d-e053-6c86abc040b9

Geist, E.L. and ten Brink, U.S., (2021) Earthquake Magnitude Distributions on Northern Caribbean Faults from Combinatorial Optimization Models, *J. Geophys. Res.*, in press.

Granja-Bruña, J. L., U. S. ten Brink, A. Carbó-Gorosabel, A. Muñoz-Martín, M. Gómez Ballesteros (2009). Morphotectonics of central Muertos thrust belt and Muertos Trough (northeastern Caribbean), *Mar. Geol.* **263** 7-33. doi:10.1016/j.margeo.2009.03.010.

Grindlay, N. R., L. J. Abrams, L. Del Greco, and P. Mann (2005). Toward an integrated understanding of Holocene fault activity in western Puerto Rico: constraints from high-resolution seismic and sidescan sonar data. Active Tectonics and Seismic Hazards of Puerto Rico, the Virgin Islands, and Offshore Areas, *Geol. Soc. Am Spec. Pap.* **385**, 139-160.

Grossman, I. G., 1963, Geology of the Guanica-Guayanilla Bay area, southwestern Puerto Rico: Art. 29 in *U.S. Geol. Survey Prof. Paper* **475-**B, p. B114-B116

Harding, T. P. (1985). Seismic characteristics and identification of negative flower structures, positive flower structures, and positive structural inversion. *AAPG Bulletin*, ***69***, 582-600.

Kaneko, Y., and Y. Fialko (2011). Shallow slip deficit due to large strike-slip earthquakes in dynamic rupture simulations with elasto-plastic off-fault response. *Geophysical Journal International*, *186*, 1389-1403.

Kaye, C.A. (1957), Notes on the structural geology of Puerto Rico, *Bull. Geol. Soc. Am.* **68** 103-118.

Liang, C., and E. J. Fielding (2017), Measuring Azimuth Deformation With L-Band ALOS-2 ScanSAR Interferometry, *IEEE Trans. Geosci. Remote Sensing* **55** 2725-2738, doi:10.1109/TGRS.2017.2653186.

Liu, C., T. Lay, T., Z. Wang, and X. Xiong (2020). Rupture process of the 7 January 2020, MW 6.4 Puerto Rico earthquake. *Geophys. Res. Lett.* **47** e2020GL087718.

López-Venegas, A.M., E. Vanacore, S. K. Hughes (2020a), Puerto Rico's Winter 2019-2020 Seismic Sequence Leaves the Island On Edge, *Temblor*, http://doi.org/10.32858/temblor.064.

López-Venegas, A.M., E. Vanacore, S. K. Hughes, G. Báez- Sánchez, and T. R. Hudgins (2020b), Response and initial scientific findings from the southwestern Puerto Rico Seismic Sequence" (2020), *Temblor*, http://doi.org/10.32858/temblor.068.

Manaker, D. M., E. Calais, A. M. Freed, S. T. Ali, P. Przybylski, G. Mattioli, P. Jansma, C. Prépetit, and J. B. De Chabalier (2008), Interseismic Plate coupling and strain partitioning in the Northeastern Caribbean, *Geophys. J. Int.* **174** 889-903 246X.2008.03819.x.

Mann, P., E. Calais, J.-C. Ruegg, C. DeMets, and P.E. Jansma, (2002) Oblique collision in the north-eastern Caribbean from GPS measurements and geological observations. *Tectonics* **21** 7-1.http://dx.doi.org/10.1029/2001TC0011304.

Mann, P., J. C. Hippolyte, N. R. Grindlay, and L. J. Abrams, (2005). Neotectonics of southern Puerto Rico and its offshore margin. Active tectonics and seismic hazards of Puerto Rico, the Virgin Islands, and offshore areas, *Geol. Soc. Am Spec. Pap.* **385**, 173-214.

Marshall, J.S., D.M. Fisher, and T.W. Gardner (2000) Central Costa Rica deformed belt: Kinematics of diffuse faulting across the western Panama block. *Tectonics* **19** 468-492.

Miranda, E. et al. (16 authors) StEER Puerto Rico M6.4 earthquake 7 January 2020 preliminary virtual reconnaissance report (PVRR), NHERI DesignSafe Project ID: PRJ-2670,Released: January 10, 2020

Monroe, W. H. (1980). Geology of the middle Tertiary formations of Puerto Rico U.S. Geological Survey Prof. Pap 953.

Morales-Velez, A.C., J. Bernal, K.S. Hughs, M. Pando, J.C. Perez, L.A. Rodriguez, and L.E. Suarez, Geotechnical Reconnaissance of the January 7, 2020 M6.4 Southwest Puerto Rico Earthquake and Associated Seismic Sequence, Geotechnical Extreme Event Reconnaissance Report (GEER)-066. June 26, 2020.

Pérez-Valentín, K., Barreto-Orta, M., Castro, A., Montañez-Acuña, A., and Cabrera-Valentín, N. (2021). Revealing geomorphic changes after the occurrence of a seismic event on the south coast of Puerto Rico (2020), *Shore and Beach*, **89**, 22-33.

Piety, L. A., J. R. Redwine, S. A. Derouin, C. S. Prentice, K. I. Kelson, R. E. Klinger, and S. Mahan (2018) Holocene Surface Ruptures on the Salinas Fault and Southeastern Great Southern Puerto Rico Fault Zone, South Coastal Plain of Puerto Rico, *Bulletin of the Seismological Society of America*, **108** 619–638, doi: 10.1785/0120170182

Pindell, J. L., and L. Kennan, (2009). Tectonic evolution of the Gulf of Mexico, Caribbean and northern South America in the mantle reference frame: an update. *Geological Society, London, Special Publications*, *328*, 1-55.

Prentice, C. S., and P. Mann (2005). Paleoseismic study of the South Lajas fault: First documentation of an onshore Holocene fault in Puerto Rico, *Geol. Soc. Am. Spec. Pap.* **385** 215–222.

Renken, R. A., B. A. Black, W. C. Ward, I. P. Gill, F. Gómez-Gómez, and J. Rodríguez-Martínez (2002). Geology and hydrogeology of the Caribbean islands aquifer system of the commonwealth of Puerto Rico and the US Virgin Islands. US Geological Survey Prof. Pap. 1419.

Roig-Silva, C. M., E. Asencio, and J. Joyce (2013). The northwest trending North Boquerón Bay-Punta Montalva fault zone—A through going active fault system in southwestern Puerto Rico, *Seismol. Res. Lett.* **84** 538–550.

Rosen, P. A., E. Gurrola, G. F. Sacco, and H. Zebker (2012), The InSAR Scientific Computing Environment, paper presented at 9th European Conference on Synthetic Aperture Radar, Nuremberg, Germany, 23-26 April.

Ross, Z. E., B. Idini, Z. Jia, O. L. Stephenson, M. Zhong, X. Wang, ... and J. Jung (2019). Hierarchical interlocked orthogonal faulting in the 2019 Ridgecrest earthquake sequence. *Science* ***366*** 346-351

Shcherbakov, R. and D.L. Turcotte (2004). A modified form of Bath's law. Bull. Seismol. Soc. Am. ***94*** 1968-1975.

Solares-Colón, M.M., (2019), New Constraints on Crustal Deformation Within the Puerto Rico-Virgin Islands Microplate Using Two Decades of GPS Data, Ms.C. thesis, University of Puerto Rico, Mayaguez.

Styron, R.H., M.H. Taylor and M.A. Murphy, 2011. Oblique convergence, arc-parallel extension, and the role of strike-slip faulting in the High Himalaya. *Geosphere*, *7*, 582-596.

Symithe, S., E. Calais, J. B. de Chabalier, R. Robertson, and M. Higgins (2015), Current block motions and strain accumulation on active faults in the Caribbean, *J. Geophys. Res.: Solid Earth*, **120** 3748-3774 https://doi.org/10.1002/2014JB011779.

ten Brink, U.S. (2005). Vertical motions in the Puerto Rico trench and Puerto Rico and their cause, *J. Geophys. Res.* **110**, B06404, doi:10.1020/2004JB003459.

ten Brink, U.S., S. Marshak, and J.-L. Granja Bruña, (2009). Bivergent thrust wedges surrounding oceanic island arcs: Insight from observations and sandbox models of the northeastern Caribbean plate, *Geol. Soc. Am. Bull.* **121** 1522-1536. doi:10.1130/B26512.1.

ten Brink, U.S., W.H. Bakun, and C.H. Flores (2011). Historical perspective on seismic hazard to Hispaniola and the NE Caribbean, *J. Geophys. Res.* **116**, B12318, doi:10.1029/2011JB008497.

ten Brink, U.S., and López-Venegas, A.M. (2012). Plate interaction in the NE Caribbean subduction zone from continuous GPS observations, *Geophys., Res. Lett*. **39**, L10304, doi:10.1029/2012GL051485.

Toda, S., Stein, R.S., Sevilgen, V., and Lin, J., 2011, Coulomb 3.3 Graphic-rich deformation and stress-change software for earthquake, tectonic, and volcano research and teaching—user guide: U.S. Geological Survey Open-File Report 2011–1060, 63 p.

Trumbull, J. V. and L.E. Garrison (1973) Geology of a system of submarine canyons south of Puerto Rico. *J. Res. U.S. Geol. Sur*. **1** 293-299.

Vanacore, E. A., Joyce, J., ten Brink, U., Fielding, E. J., López-Venegas, A. (2021) Double Difference relocations of the Southwestern Puerto Rico Seismic Sequence, *Seis. Res. Lett.*, 92, 1444.

von Hillebrandt-Andrade, C. G, A. López-Venegas, E. Vanacore (2020), 2019-2020 Southwestern Puerto Rico Seismic Sequence, *TsuInfo Alert*, **22**, no. 1.

Waldhauser, F., & Ellsworth, W. L. (2000). A double-difference earthquake location algorithm: Method and application to the northern Hayward fault, California. Bulletin of the Seismological Society of America, 90(6), 1353-1368.

Wells, D.L., and K.J. Coppersmith (1994) New Empirical Relationships among Magnitude, Rupture Width, Rupture Area, and Surface Displacement, Seismol. Soc. Am. 84 974–1002.

Withjack, M. O., Q. T. Islam and P.R. La Pointe (1995). Normal faults and their hanging-wall deformation: an experimental study. *AAPG bull.* **79** 1-17.

Wright, T. J., B. E. Parsons, and Z. Lu (2004). Toward mapping surface deformation in three dimensions using InSAR, Geophysical Research Letters **31** L01607.

Yunjun, Z., H. Fattahi, and F. Amelung (2019), Small baseline InSAR time series analysis: Unwrapping error correction and noise reduction, *Computers & Geosciences* **133** 104331, doi:10.1016/j.cageo.2019.104331.

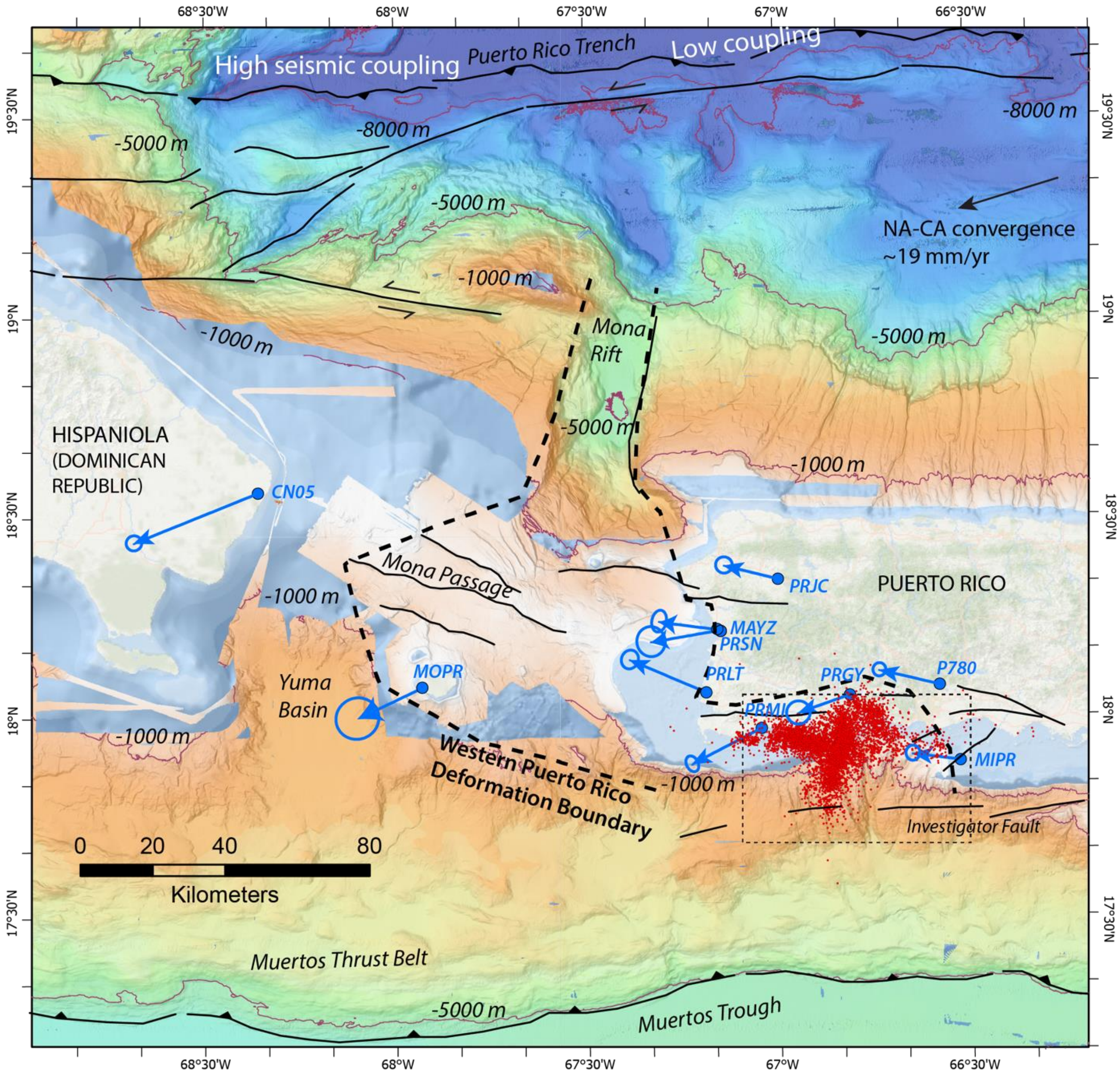

Figure 1. *Regional map. Shaded multibeam bathymetry (Andrews et al.,* 2014*) colored by water depth with selected depth contours (thin purple lines. Areas without multibeam bathymetry from GEBCO global bathymetry and are shaded light blue. Red dots – M ≥ 2.5 earthquakes in the SWPR seismic sequence from ANSS-ComCat. Black lines – Major faults after Geist and ten Brink (*2021*). Blue lines- GPS vectors with length proportional to long-term velocities relative to fixed Caribbean plate from the Nevada Geodetic laboratory (Table A2). Area between dashed*

lines is our proposed Western Puerto Rico Deformation Boundary. dotted black rectangle – Location of Fig. 2.

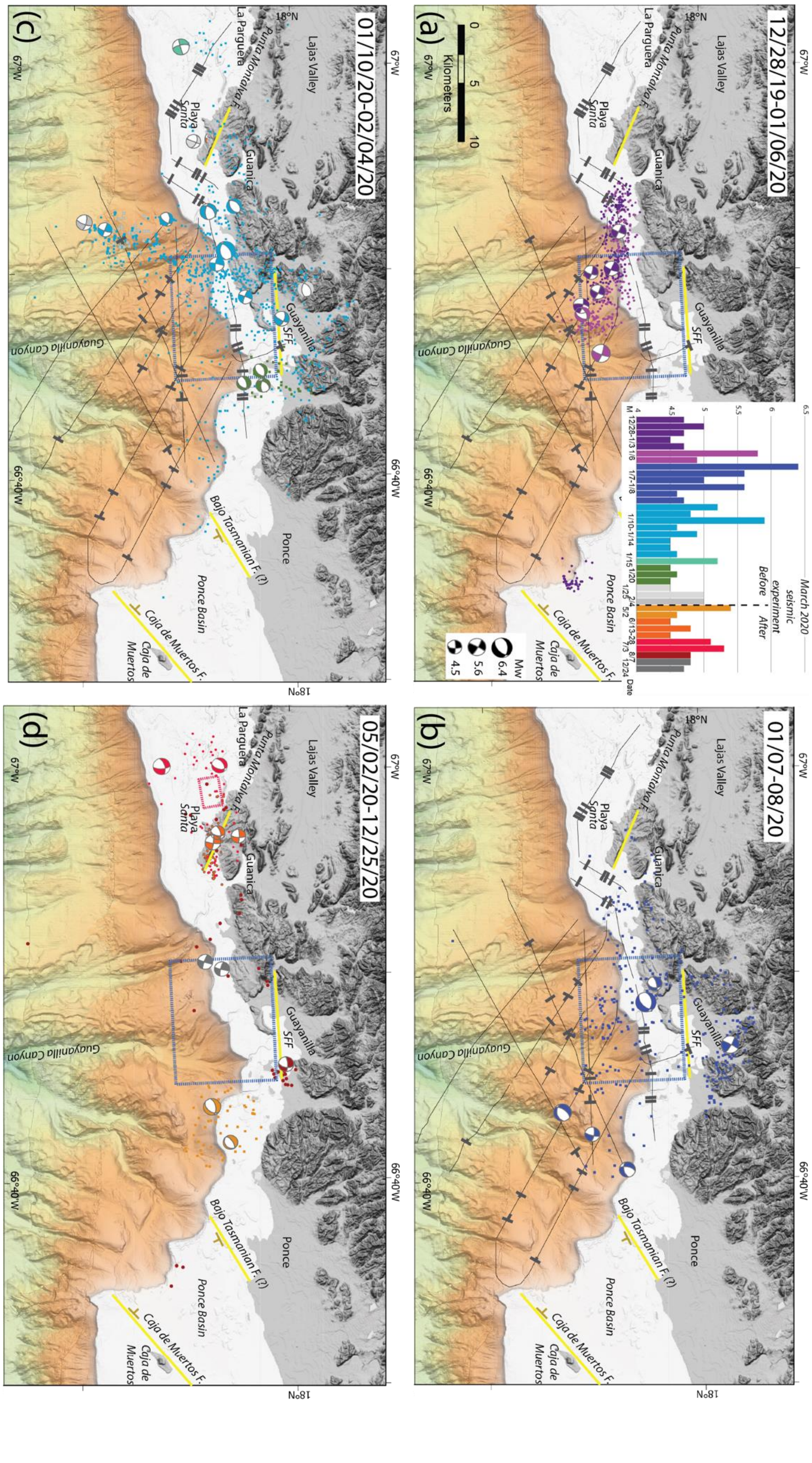

(a) 12/28/19-01/06/20
(b) 01/07-08/20
(c) 01/10/20-02/04/20
(d) 05/02/20-12/25/20
Lajas Valley
Punta Montalva F.
La Parguera
Playa Santa
Guanica
Guayanilla
SFF
Guayanilla Canyon
Ponce
Bajo Tasmanian F. (?)
Ponce Basin
Caja de Muertos F.
Caja de Muertos
18°N
67°W
66°40'W
Kilometers
0
5
10
M
Date
March 2020 seismic experiment
Before
After
Mw
6.4
5.6
4.5

Figure 2 Locations and focal mechanisms of Mw≥4.5 earthquake clusters (from ANSS-ComCat) colored by date. Inset shows dates of the clusters and color code. Grey earthquakes are moderate earthquakes not associated with a cluster. Some alternate epicenters from the catalog are shown, as discussed in the text and listed in Table A1. Colored dots – Relocated microseismicity using HypoDD (Vanacore et al, 2021*) for a few selected dates, with colors matching the dates of focal mechanisms and the inset. Thin lines – locations of seismic reflection profiles collected between 03/07-03/13/2020, Heavy black marks – Faults interpreted from the seismic reflection profiles with small perpendicular marks denoting apparent dip direction. Dotted rectangles – Modeled fault planes from the InSAR observations (Figs. 5 and 6) with colors matching the dates of the focal mechanisms and inset. Yellow lines – published faults. Background – Shaded bathymetry colored by depth (white -100 m to blue – 2000 m) and SRTM hill-shaded topography (grey). SFF – San Francisco Fault.*

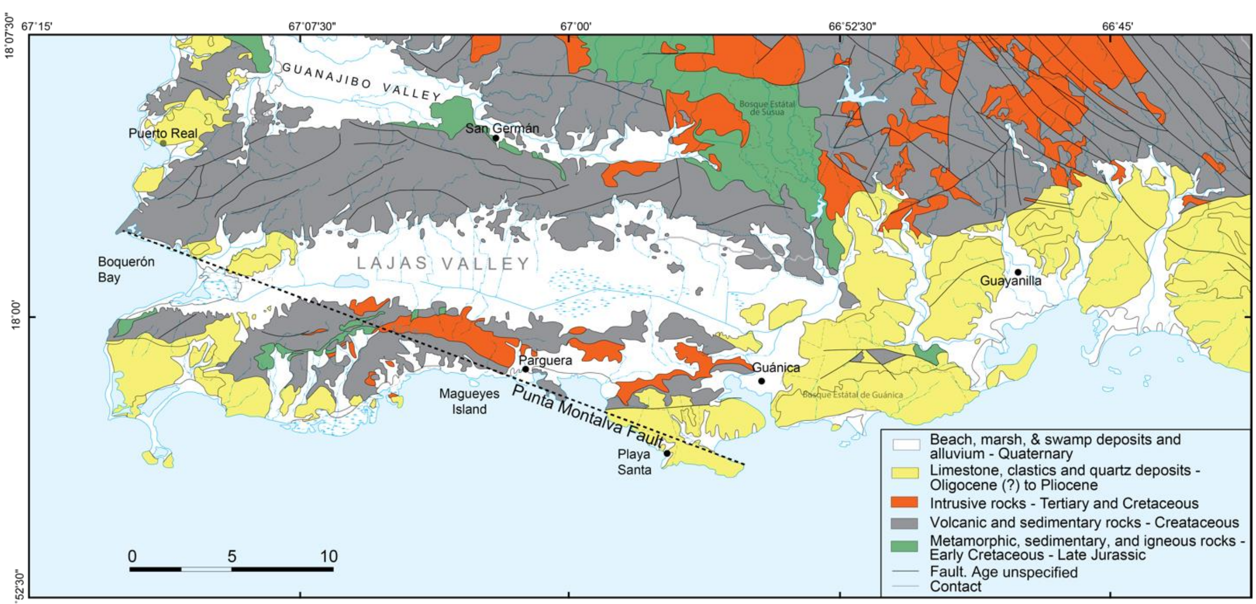

***Figure 3.** Simplified geological map of SWPR modified from* Renken et al. (2002). *Dotted line – proposed 33-km-long Punta Montalva Fault by* Roig-Silva et al., (2013).

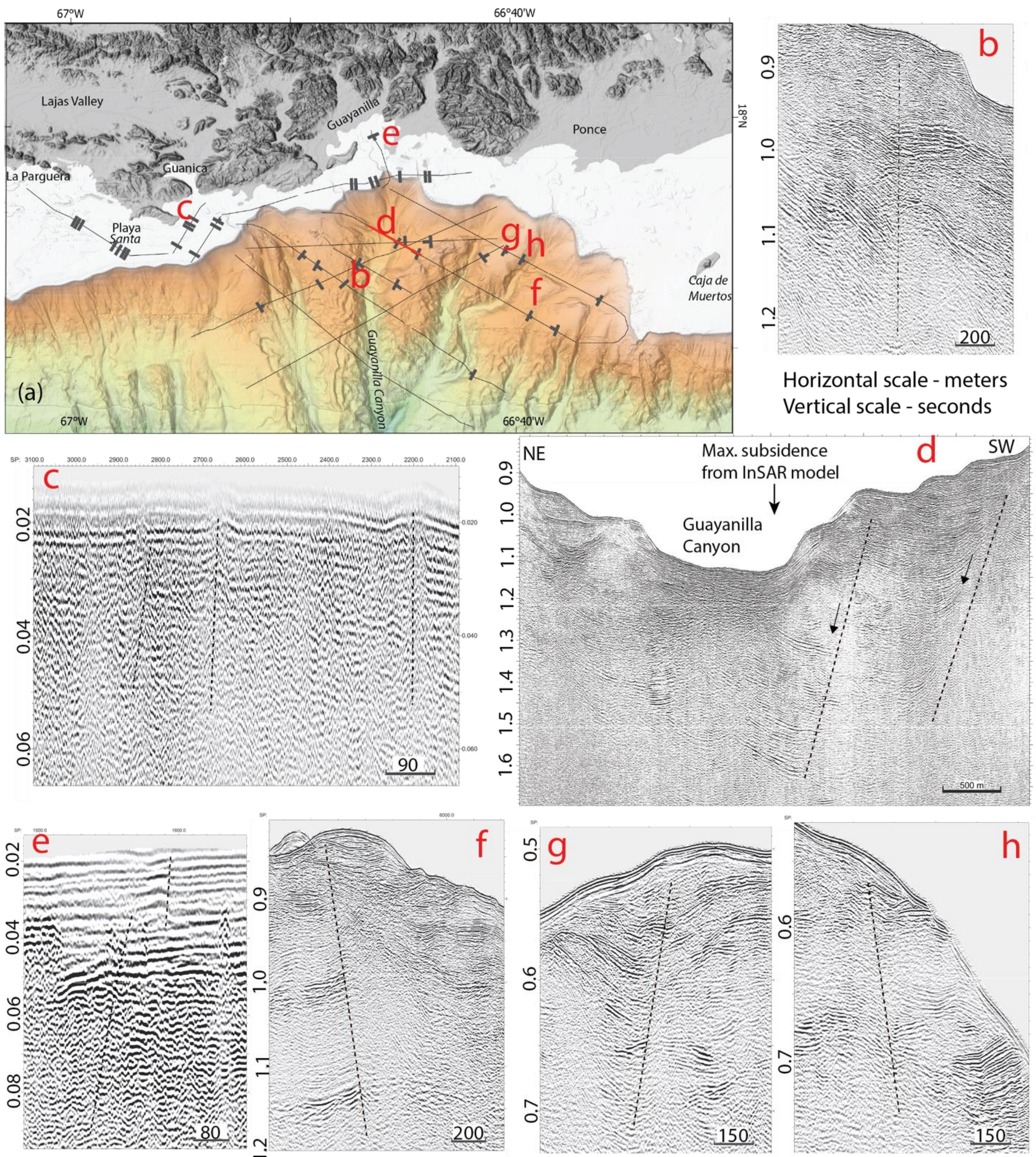

Figure 4. *(a) – Location map of seismic records shown in (b)-(h). Red line shows extent of profile (d). (b)-(h) examples of interpreted faults (dashed lines). (d) – tilted reflectors toward the faults. The maximum sediment thickness is coincident with the region of maximum subsidence predicted by the Mw6.4 subsidence model. White area on map (a) is the shelf with water depths*

<100 m, above which limited sound source output was used and seafloor was typically made of hard coral reef. Thin lines in (a) – locations of seismic reflection profiles. Heavy black marks in (a) – Interpreted faults on the seismic reflection profiles with small perpendicular marks denoting apparent dip direction. Vertical scale of *0.1 s of two-way travel time in (b)-(h) corresponds roughly to 100 m in the sub-seafloor.*

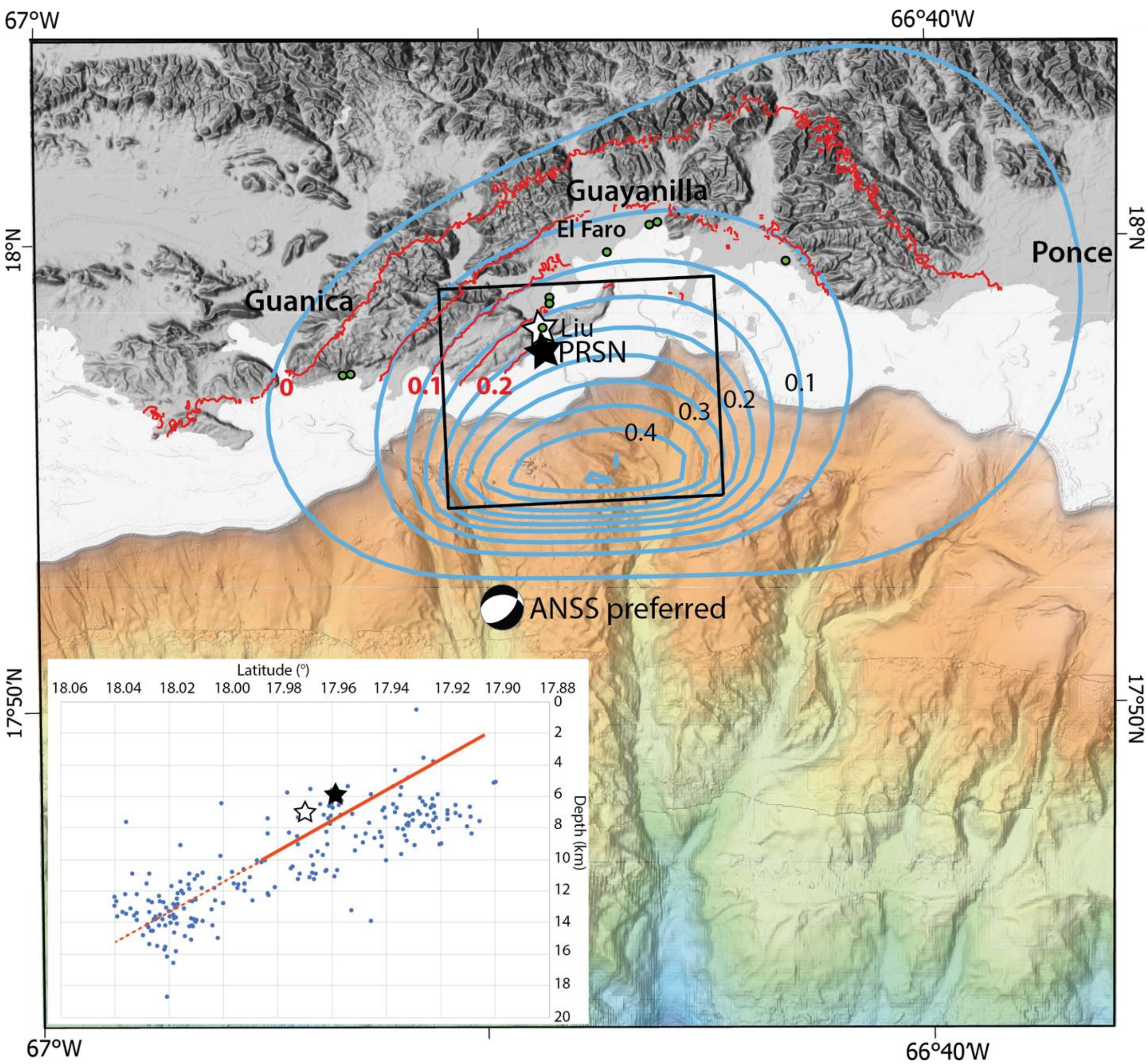

Figure 5. *Comparison between InSAR subsidence observations for the period* 01/02-01/14/2020 ***(****red contours) and a subsidence model (blue contours). Contour interval for both is 0.05 m. Black rectangle -Surface projection of the modeled fault plane. The fault plane dips 43° to the north. See text and Table A3 for modeled fault parameters. Note that the preferred epicenter in the ANSS-ComCat is 5 km south of the updip edge of the fault plane, whereas the PRSN epicenter is located toward the bottom of the fault patch. Liu –* Liu et al. (2020) *epicenter (*17.97°N, 66.81°W)*. Green dots – reported locations of coastal subsidence following the earthquake. Inset -Projection of relocated small earthquakes by* Vanacore et al. (2021) *occurring within the longitudes of the modeled fault patch during 01/07-01/08/2020. Red line is our modeled fault plane. Dashed red line is an extrapolation to deeper depths. Black and white stars - Projected hypocenters of PRSN and Liu et al. respectively.*

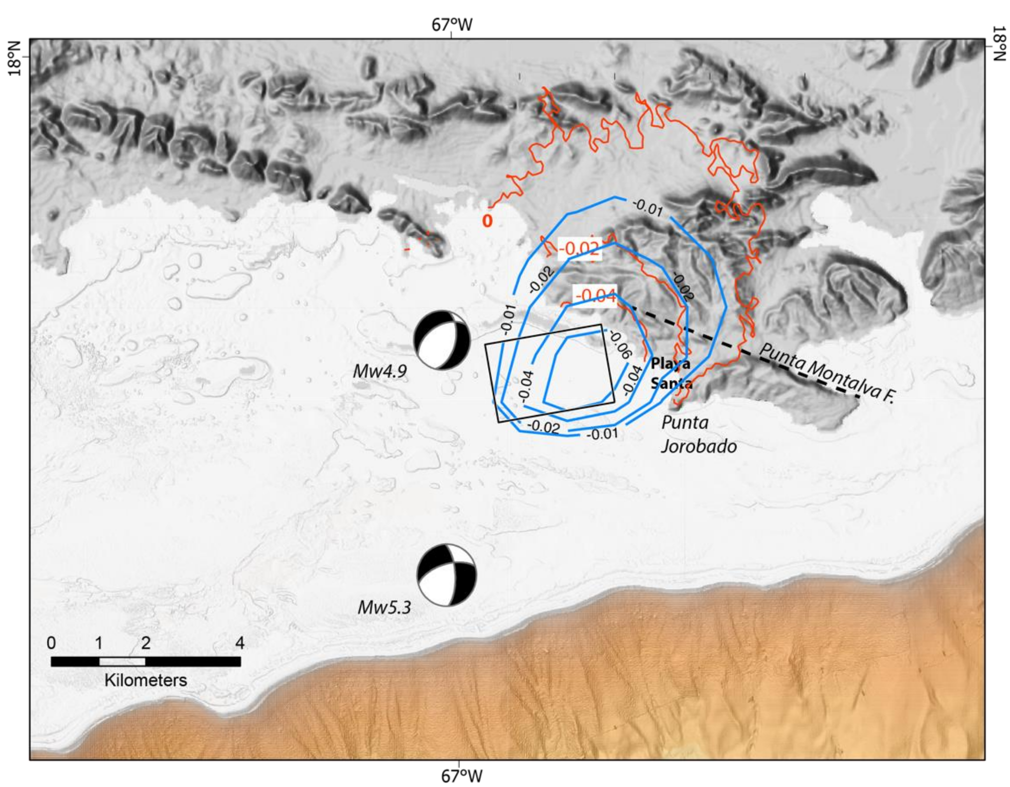

Figure 6. *Comparison between InSAR subsidence observations during the period of 07/02-07/12 (Red contours) and modeled subsidence using the ANSS-ComCat focal plane parameters for the Mw5.3 (blue contours). Contour interval for both is 0.02 m. Black rectangles - Surface projection of the modeled fault plane. Fault plane dips to the NW. See text and* Table A3 *for modeled fault parameters. Beach balls - Alternate focal mechanisms for the two* 07/03/2020 *earthquakes are from ANSS-ComCat listed in* Table A3.

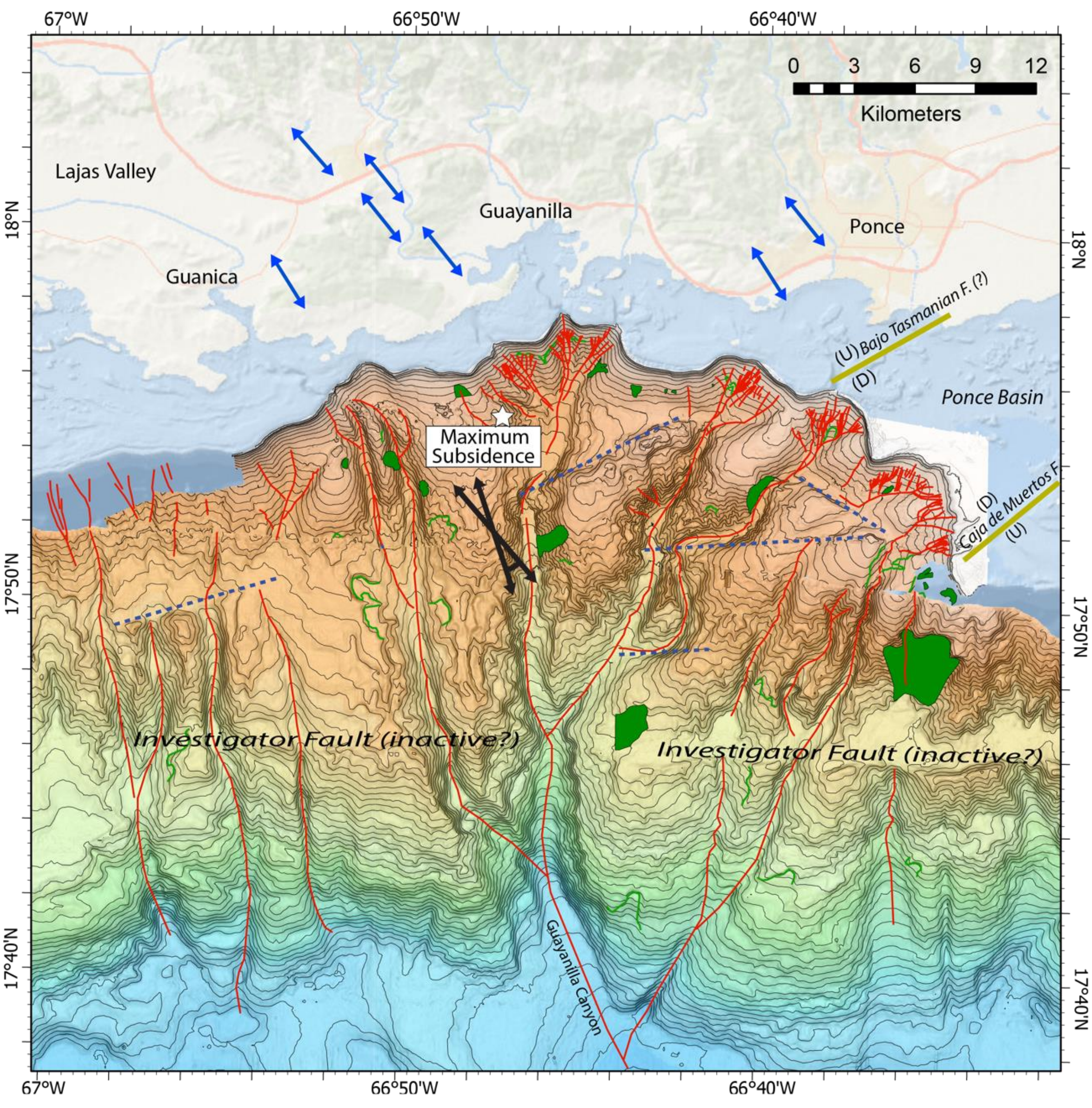

Figure 7. *Compilation of evidence suggestive of long-term seismic activity in the study area. Dark double-sided arrows – Extension directivity of a range of T-axes for Mw>4.5 earthquakes in the seismic sequence (shown offshore) (See Table A1). Double-sided blue arrow – Extension directions from terrestrial post Early-Pliocene fault striations (Mann et al.,* 2005*). Yellow lines – mapped faults enclosing a several hundred milliseconds thick Ponce half graben and their sense of motion (Garrison,* 1969*). Star - Center of modeled subsidence in Fig. 5. Blue dashed lines - Seafloor lineaments disrupting drainage on an otherwise general southward slope indicating possible tectonic control. Red lines – Thalwegs of the drainage system. Green areas – Landslide scars. Green lines – Landslide scarps. Guayanilla Canyon is the only large submarine canyon along southern Puerto Rico, and it eroded the shelf to within 1 km from shore.*

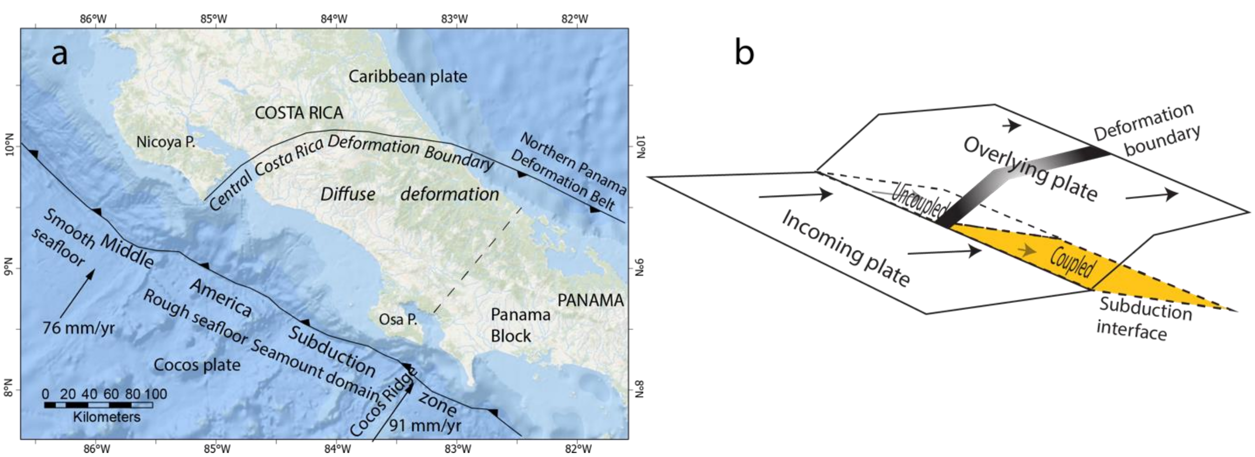

Figure 8. *(a) Simplified map of the Central Costa Rica Deformation Boundary (Marshall et al,* 2000*), a diffuse block boundary, an analogous setting to the Western Puerto Rico Deformation Boundary. (b)Cartoon showing the impact of seismic coupling along the subduction interface on differential velocity of the overlying arc relative to the overlying plate interior. The coupled and uncoupled subduction interfaces are the Hispaniola and Puerto Rico segments, respectively, and are separated by a deformation zone north of Mona rift. In Central America, the coupled and*

uncoupled subduction interfaces correspond to the rough and smooth seafloor of the incoming Cocos plate (a).

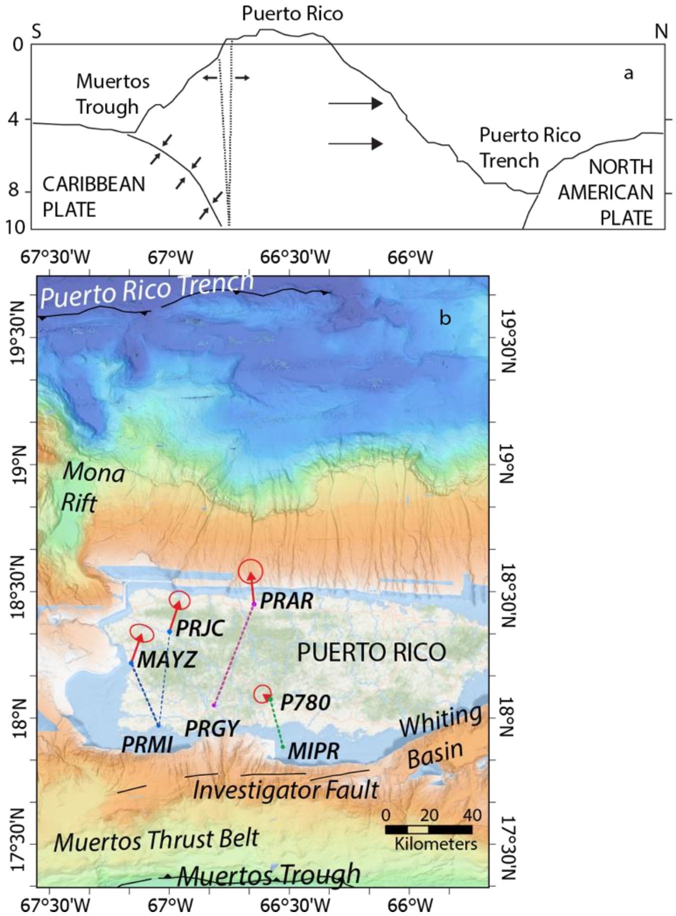

Figure 9. *(a) An alternative explanation to the recent seismic activity in which fusion of the southern edge of the Puerto Rico block with the Caribbean plate may cause extension to develop along southwest Puerto Rico. (b) Velocity differences between GPS stations across Puerto Rico (Table A2). Red arrows show velocity vectors of stations relative to stations located farther south, with whom they are connected by dashed lines.*

Supplemental material for the article

Mature diffuse tectonic block boundary revealed by the 2020 southwestern Puerto Rico seismic sequence

By U.S. ten Brink, L. Vanacore, E.J. Fielding, J.D. Chaytor, A.M. López-Venegas, W. Baldwin[1], D. Foster, B.D. Andrews

The supplemental material includes lists of earthquake and GPS data plotted in Figures 1 and 2 and a list of bathymetry sources used to make the background bathymetry in Figures 1, 2, 4A, 5, 6, and 7.

Table A1 Mw≥4.5 from the ANSS-ComCat (https://earthquake.usgs.gov/earthquakes/search/) shown in Figure 2

yrmodayhrmin	Pref. lon (°W)	Pref. lat (°N)	Alt lon (°W)	Alt Lat (°N)	Moment (N-m)	Mw	Depth (km)	T axis (°)
201912282235	66.866	17.937			1.15E+16	4.7	6	340
201912290106	66.864	17.885	66.806	17.907	2.29E+16	5	6	156
201912290121	66.836	17.931			1.46E+16	4.7	3	341
202001022042	66.833	17.915			6.84E+15	4.5	7	333
202001030341	66.826	17.901	66.817	17.920	1.68E+16	4.7	2	161
202001061032	66.819	17.868	66.767	17.922	3.17E+17	5.8	6	156
200001061451	66.799	17.908			8.71E+15	4.9	6	318
202001070824	66.827	17.869	66.811	17.958	5.04E+18	6.4	9	156

202001070834	66.722	17.892			3.11E+17	5.6	10	325
202001070850	66.675	17.942			3.54E+16	5	10	313
202001071118	66.776	18.022			3.63E+17	5.6	9	164
202001071627	66.826	17.965			4.52E+15	4.6	8	320
202001082004	66.704	17.915			6.38E+15	4.7	6	147
202001102226	66.883	17.935	66.850	17.943	5.82E+16	5.2	9	161
202001110228	66.795	17.992			1.15E+16	4.8	4	158
202001111254	66.851	17.949			1.06E+18	5.9	5	339
202001112349	66.840	17.942			7.85E+15	4.6	8	325
202001120759	66.887	17.956			7.33E+15	4.9	8	143
202001121055	66.877	17.903			2.52E+15	4.5	7	335
202001130520	66.813	17.964			6.60E+15	4.5	9	335
202001141226	66.869	17.855			1.87E+16	4.6	10	336
202001151536	67.017	17.916			4.87E+16	5.2	5	123
202001200526	66.741	17.977			5.76E+15	4.5	7	157
202001200936	66.753	17.975			3.43E+15	4.6	7	149
202001201514	66.743	17.962			4.52E+15	4.5	14	327
202001250800	66.940	17.925			2.25E+15	4.5	6	152
202001252020	66.819	18.011			1.41E+16	5	13	164
202002041455	66.875	17.839			2.92E+16	5	7	153
202005021113	66.727	17.937			1.38E+17	5.4	9	332
202005021119	66.698	17.951			5.76E+15	4.6	7	325
202006130552	66.947	17.960			3.09E+15	4.5	9	317

202006280642	66.942	17.940			2.04E+16	4.8	11	322
202006282248	66.950	17.944			2.79E+15	4.5	13	315
202007031354	67.004	17.944			6.62E+16	4.9	6	129
202007032049	67.005	17.900			8.22E+16	5.3	3	126
202008070327	66.761	17.995			1.11E+16	4.8	12	325
202012241656	66.845	17.933			1.23E+16	4.8	6	334
202012241733	66.839	17.946			3.42E+15	4.7	9	328

Note: Pref. longitude and latitude are the preferred location provided in the catalog. Alt lon and lat are alternative locations listed for these events

Table A2. GPS motion relative to a fixed Caribbean plate from the MAGNET GPS network (http://geodesy.unr.edu/magnet.php) shown in Figure 1

Station	Long (°W)	Lat (°N)	speed (mm/y)	Azimuth (°)	East (mm/y)	North (mm/y)	Error E (mm/y)	Error N (mm/y)	Start & end dates
CN05	68.359	18.564	4.641	248	-4.310	-1.721	0.27	0.26	2014-2020
MOPR	67.931	18.077	2.508	245	-2.268	-1.071	0.75	0.71	10/08-8/11 11/14-8/16
PRMI	67.045	17.97	2.728	243	-2.432	-1.236	0.2	0.29	2016-2015
PRGY	66.814	18.051	1.907	251	-1.804	-0.618	0.41	0.4	2011-2019
MAYZ	67.159	18.218	2.042	278	-2.023	0.276	0.25	0.38	2010-2015
PRSN	67.145	18.217	2.528	261	-2.493	-0.417	0.49	0.52	2015-2019
PRLT	67.189	18.060	2.885	293	-2.604	1.126	0.29	0.33	2010-2019
PRJC	66.999	18.342	1.936	284	-1.876	0.479	0.29	0.28	2010-2019
PRAR	18.45	-66.647	2.312	300	-1.993	1.172	0.24	0.26	2010-2019
MIPR	66.527	17.886	1.679	278	-1.663	0.228	0.24	0.26	2008-2016
P780	66.579	18.075	2.159	284	-2.099	0.509	0.22	0.23	2008-2018

Notes:

1. Data after 12/227/2019 (the beginning of the 2019-2020 seismic sequence) was excluded from the stations in Puerto Rico, because of abrupt velocity changes in response to the seismic sequence.

2. Errors were calculated using the MIDAS trend estimator (Blewitt, G., C. Kreemer, W.C. Hammond, and J. Gazeaux, 2016, MIDAS robust trend estimator for accurate GPS station velocities without step detection, *J. Geophys. Res.*, 121, doi:10.1002/2015JB012552) and posted at the Nevada Geodetic Laboratory website http://geodesy.unr.edu/magnet.php

Table A3. Parameters of elastic models to match InSAR subsidence observations in Fig. 5 and 6.

(a) Models to match the 01/07/2020 Mw6.4 subsidence

Model #	Fault length (km)	Fault width (km)	top depth (km)	bottom depth (km)	Strike (°)	dip (°)	rake (°)	slip (m)	Moment (x E18 N-m)***
1*	7.64	14.66	2	12	268	43	-58	1.50	5.04
2*	11.46	14.66	2	12	268	43	-58	1.00	5.04
3	15.08	11.73	2	10	268	43	-65	0.95	5.04
4	12.73	13.20	3	12	268	43	-68	1.00	5.04
5	9.55	17.60	2	14	268	43	-68	1.00	5.04
6	11.46	14.66	2	12	268	43	-68	1.00	5.04
7	11.46	14.66	3	13	268	43	-68	1.00	5.04
8	12.78	13.20	3	12	268	43	-68	1.00	5.04
9	11.49	15.40	1.5	12	268	43	-68	0.95	5.04
10	10.42	14.66	2	12	268	43	-68	1.10	5.04
11	14.32	11.73	2	10	268	43	-68	1.00	5.04
12	12.73	13.20	2	11	268	43	-70	1.00	5.04
13	14.32	11.73	2	10	268	43	-70	1.00	5.04
14**	**11.32**	**11.73**	**2**	**10**	**268**	**43**	**-72**	**1.26**	**5.04**
15	14.32	11.73	2	10	268	43	-75	1.00	5.04
16	17.90	11.73	2	10	268	43	-75	0.80	5.04
17	14.32	11.73	2	10	268	43	-80	1.00	5.04
18	15.91	11.73	2	10	268	43	-90	0.90	5.04

* ANSS-ComCat preferred focal plane solution for the 202001070824 Mw6.4

** Parameters of model shown in Fig. 5

*** Seismic moment from ANSS-ComCat for the event

(b) Additional models to match the 01/07/2020 Mw6.4 subsidence ignoring the seismic moment constraint

Model #	Fault length (km)	Fault width (km)	top depth (km)	bottom depth (km)	Strike (°)	dip (°)	rake (°)	slip (m)	Moment (x E18 N-m)
1	11.46	11.73	2.0	10.0	268	43	-58	1.00	4.03
2	12.29	14.66	2.0	12.0	268	43	-58	1.00	5.40
3	7.91	14.66	2.0	12.0	268	43	-68	1.00	3.48
4	11.32	11.73	2.0	10.0	268	43	-68	1.00	3.98
5	11.79	16.13	2.0	13.0	268	43	-70	0.75	4.28
6	11.32	11.73	2.0	10.0	268	43	-70	1.00	3.99
7	12.16	11.73	2.0	10.0	268	43	-70	1.00	4.28
8	12.38	11.73	2.0	10.0	268	43	-70	1.00	4.36
9	11.32	16.13	2.0	13.0	268	43	-72	1.26	6.93
10	11.32	19.06	2.0	15.0	268	43	-72	1.26	8.19
11	11.32	11.73	2.0	10.0	268	43	-72	1.00	3.98
12	13.14	12.46	3.5	12.0	268	43	-75	1.10	5.41
13	9.64	12.46	3.5	12.0	268	43	-75	1.50	5.40
14	8.20	14.66	3.0	13.0	268	43	-75	1.50	5.41
15	10.25	11.73	4.0	12.0	268	43	-75	1.50	5.41
16	12.05	12.46	3.5	12.0	268	43	-80	1.20	5.41
17	16.12	9.81	4.0	12.5	225	60	-82	0.71	3.36
18	10.00	13.20	3.0	12.0	270	43	-68	1.00	3.96
19	10.00	14.66	2.0	12.0	270	43	-68	1.00	4.40

(c) Models to match the 07/03/2020 InSAR subsidence

Model #	Fault length (km)	Fault width (km)	top depth (km)	bottom depth (km)	Strike (°)	dip (°)	rake (°)	slip (m)	Moment (x E16 N-m)	Note
1	1.31	5.18	1.0	6.0	260	75	-10	0.41	8.22	1
2	2.18	3.11	0.5	3.5	260	75	-10	0.41	8.22	1
3	1.53	5.72	1.0	6.0	254	61	-27	0.41	10.60	2
4	2.54	3.43	2.0	5.0	254	61	-27	0.41	10.60	2
5	1.09	8.00	0.5	7.5	254	61	-27	0.41	10.60	2
6	1.91	4.57	0.5	4.5	254	61	-27	0.41	10.60	2
7	1.53	5.72	0.5	5.5	254	61	-27	0.41	10.60	2
8*	**2.54**	**3.43**	**0.5**	**3.5**	**254**	**61**	**-27**	**0.41**	**10.60**	**2**
9	1.07	8.27	3.5	5.5	239	14	-65	0.25	6.62	3
10	1.59	4.64	2.0	5.5	239	49	-57	0.30	6.62	4
11	1.85	3.98	0.5	3.5	239	49	-57	0.30	6.62	4
12	2.22	3.31	0.5	3.0	239	49	-57	0.30	6.62	4
13	1.59	4.64	0.5	4.0	239	49	-57	0.30	6.62	4

* Parameters of model shown in Fig. 6

Notes:

1. ANSS-ComCat preferred focal plane solution and seismic moment for the 202007032049 Mw5.3 earthquake

2. ANSS-ComCat alternative focal plane solution and seismic moment for the 202007032049 Mw5.3 earthquake

3. ANSS-ComCat preferred focal plane solution and seismic moment for the 202007031354 Mw4.9 earthquake

4. ANSS-ComCat alternative focal plane solution and seismic moment for the 202007031354 Mw4.9 earthquake

Appendix A4 – Bathymetry sources used to plot Figures 1, 2, 4A, 5, 6, and 7

Cooperative Institute for Research in Environmental Sciences (CIRES) at the University of Colorado, Boulder. 2014: Continuously Updated Digital Elevation Model (CUDEM) - 1/9 Arc-Second Resolution Bathymetric-Topographic Tiles. [customized subset download bound by coordinates 67.125 W, 18.166 N, 66.125 W, and 17.751 N]. NOAA National Centers for Environmental Information, accessed March 16, 2021, at https://doi.org/10.25921/ds9v-ky35.

National Oceanic and Atmospheric Administration, 2006, Descriptive report, habitat and hydrographic mapping survey WH00200, Puerto Rico, Northeast Caribbean Sea, vicinity of La Parguera: National Oceanic and Atmospheric Administration descriptive report, variously paged, accessed March 16, 2021, at https://www.ngdc.noaa.gov/nos/W00001-W02000/W00200.html.

National Oceanic and Atmospheric Administration, 2016, Descriptive report, navigable area mapping survey H12935, Puerto Rico, Caribbean Sea, southeast coast of Puerto Rico: National Oceanic and Atmospheric Administration descriptive report, variously paged, accessed March 16, 2021, at https://www.ngdc.noaa.gov/nos/H12001-H14000/H12935.html.

National Oceanic and Atmospheric Administration, 2018a, Descriptive report, habitat mapping survey WH00468, Puerto Rico, Northeast Caribbean Sea, vicinity of Guanica and Ponce: National Oceanic and Atmospheric Administration descriptive report, variously paged, accessed March 16, 2021, at https://www.ngdc.noaa.gov/nos/W00001-W02000/W00468.html.

National Oceanic and Atmospheric Administration, 2018b, Descriptive report, navigable area mapping survey H13143, Puerto Rico, San Juan and Ponce vicinities, Bahia de Ponce: National Oceanic and Atmospheric Administration descriptive report, variously paged, accessed March 16, 2021, at https://www.ngdc.noaa.gov/nos/H12001-H14000/H13143.html.

National Oceanic and Atmospheric Administration, 2018c, Descriptive report, navigable area mapping survey H13144, Puerto Rico, San Juan and Ponce vicinities, 8.5 NM SE of Bahia de Ponce: National Oceanic and Atmospheric Administration descriptive report, variously paged, accessed March 16, 2021, at https://www.ngdc.noaa.gov/nos/H12001-H14000/H13144.html.

Figure 4.

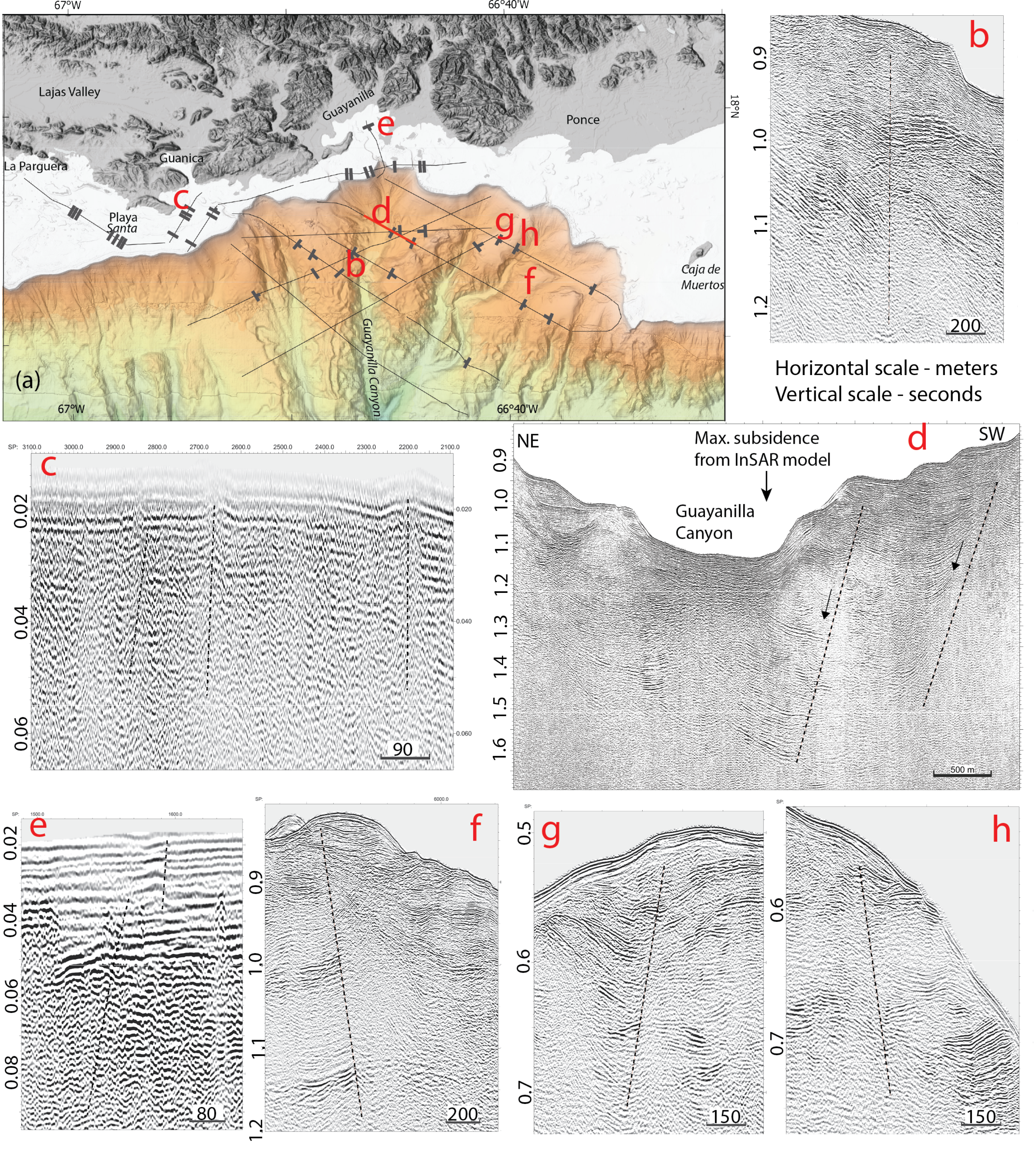

67°W
66°40'W
18°N
Lajas Valley
Guayanilla
Ponce
La Parguera
Guanica
Playa
Santa
Caja de
Muertos
Guayanilla Canyon
(a)
b
c
d
e
f
g
h
200
Horizontal scale - meters
Vertical scale - seconds
NE
SW
Max. subsidence
from InSAR model
Guayanilla
Canyon
500 m
90
80
200
150
150